Structure and dynamics of cholesterol-mediated aquaporin-0 arrays

and implications for lipid rafts

Po-Lin Chiu[1,2,%], Juan D. Orjuela[3,4,%], Bert L. de Groot[5], Camilo Aponte-Santamaría[3,6,*], and

Thomas Walz[1,7,*,#]

[1] Department of Cell Biology, Harvard Medical School, Boston, MA 02467, USA

[2] Current address: School of Molecular Sciences, Biodesign Center for Applied Structural

Discovery, Arizona State University, Tempe, AZ 85287, USA

[3] Max Planck Tandem Group in Computational Biophysics, Universidad de los Andes, Bogotá,

Colombia

[4] Biomedical Engineering Department, Universidad de los Andes, Bogotá, Colombia

[5] Computational Biomolecular Dynamic Group, Max Planck Institute for Multidisciplinary

Sciences, Göttingen, Germany

[6] Molecular Biomechanics, Heidelberg Institute for Theoretical Studies, Heidelberg, Germany

[7] Current address: Laboratory of Molecular Electron Microscopy, The Rockefeller University,

New York, NY 10065, USA; Biogen, Cambridge, MA 02142, USA

[%] These authors contributed equally.

[*] For correspondence: camilo.aponte@h-its.org, twalz@rockefeller.edu

[#] Lead Contact

Abstract

Aquaporin-0 (AQP0) tetramers form square arrays in lens membranes through a yet unknown mechanism, but lens membranes are enriched in sphingomyelin and cholesterol. Here, we determined electron crystallographic structures of AQP0 in sphingomyelin/ cholesterol membranes and performed molecular dynamics (MD) simulations to establish that the observed cholesterol positions represent those seen around an isolated AQP0 tetramer and that the AQP0 tetramer largely defines the location and orientation of most of its associated cholesterol molecules. At a high concentration, cholesterol increases the hydrophobic thickness of the annular lipid shell around AQP0 tetramers, which may thus cluster to mitigate the resulting hydrophobic mismatch. Moreover, neighboring AQP0 tetramers sandwich a cholesterol deep in the center of the membrane. MD simulations show that the association of two AQP0 tetramers is necessary to maintain the deep cholesterol in its position and that the deep cholesterol increases the force required to laterally detach two AQP0 tetramers, not only due to protein–protein contacts but also due to increased lipid–protein complementarity. Since each tetramer interacts with four such 'glue' cholesterols, avidity effects may stabilize larger arrays. The principles proposed to drive AQP0 array formation could also underlie protein clustering in lipid rafts.

Introduction

The current view of biological membranes is that proteins are densely packed and often organized into functional modules that perform specific biological functions (Engelman, 2005; Nicolson, 2014). Lipids play an important role in organizing membrane proteins, and the resulting specialized membrane domains are now commonly known as lipid microdomains or

2

lipid rafts (Karnovsky et al., 1982; Lingwood and Simons, 2010; Simons and Ikonen, 1997; Simons and Toomre, 2000; Stier and Sackmann, 1973; Vereb et al., 2003).

Lipid microdomains are enriched in cholesterol (Barenholz, 2002; Korade and Kenworthy, 2008; Simons and Ikonen, 1997) and characterized by a lipid phase that is distinct from the surrounding membrane (Ahmed et al., 1997; Schroeder et al., 1991). Cholesterol has a planar four-aromatic ring structure with a short isooctyl alkyl chain and a small 3-β-hydroxyl head group that can form a hydrogen bond with a polar group (Figure 1–figure supplement 1A). Because the aliphatic groups linked to the ring system are asymmetrically distributed, cholesterol features a smooth (or α) face and a rough (or β) face (Figure 1–figure supplement 1A). It makes up 40-90% of the lipids is eukaryotic cell membranes (Liscum and Munn, 1999; van Meer et al., 2008). Cholesterol can form non-covalent interactions with lipid acyl chains, preferentially with saturated ones (Epand and Epand, 2004; Zheng et al., 2007). As a result, the membrane can transition from a liquid-disordered to a liquid-ordered phase (de Meyer et al., 2010; Ghysels et al., 2019; Marsh, 2010; Seelig, 1977), which has been linked to the formation of lipid microdomains (Quinn and Wolf, 2009; Silvius, 2003).

Mammalian lens membranes contain a high percentage of sphingomyelin – a lipid consisting of a phosphocholine head group, a sphingosine amino alcohol and a fatty acid (Figure 1–figure supplement 1B) – and cholesterol, lipids that are characteristic for lipid rafts (Simons and Ikonen, 1997; Zelenka, 1984). With a molar ratio of cholesterol to other phospholipids ranging from 2.02 to 2.52, the human lens core plasma membrane features the highest molar cholesterol content of all membranes found in human tissues (Fleschner and Cenedella, 1991; Zelenka, 1984). Aquaporin-0 (AQP0), a lens-specific water channel, is the most abundant membrane protein in lens membranes (over 60% of the total protein content) (Alcalá et al., 1975;

Bloemendal et al., 1972), where it forms large 2D arrays (Gorin et al., 1984; Kistler and Bullivant, 1980; Zampighi et al., 1982).

The propensity of AQP0 to form 2D crystals was used to determine its structure by electron crystallography of *in vitro* assembled 2D crystals grown with the lipid dimyristoyl phosphatidylcholine (DMPC) (Gonen et al., 2005). Later, AQP0 2D crystals were grown with a variety of different lipids (Hite et al., 2015, 2010). All these crystals had the same lattice constants, which were identical to those of AQP0 arrays in native lens membranes (Buzhynskyy et al., 2007). Thus, *in vitro* grown 2D crystals recapitulate the organization of AQP0 tetramers in 2D arrays in the native lens membrane. Interestingly, however, high-resolution electron crystallographic studies, which also resolved the annular lipids (Gonen et al., 2005; Hite et al., 2010), showed that AQP0 tetramers in the 2D crystals are separated by a layer of lipids and form essentially no direct protein–protein interactions. As the crystal contacts are almost exclusively mediated by lipids, it is surprising that AQP0 2D crystals could be obtained with almost every lipid tested.

Molecular dynamics (MD) simulations further advanced our understanding of how lipids interact with AQP0. Initial simulations probing the interactions of AQP0 with lipids were carried out with pure DMPC and mixed DMPC:cholesterol membrane patches, predicting the existence of a cholesterol hotspot at the extracellular side of the AQP0 surface (O'Connor and Klauda, 2011). Later, MD simulations demonstrated that the positions of lipids around AQP0 seen in electron crystallographic structures obtained from 2D crystals, in which the lipids are constrained by the protein crystal packing, are indeed representative of the localization of unconstrained lipids around individual AQP0 tetramers (Aponte-Santamaría et al., 2012). Molecular aspects, such as protein mobility and surface roughness, were identified to play key roles in defining the

lipid positions (Aponte-Santamaría et al., 2012; Briones et al., 2017). Furthermore, a combination of coarse-grained and atomistic MD simulations revealed that annular lipids adopt similar positions around several members of the aquaporin family (Stansfeld et al., 2013), while mass spectrometry demonstrated the weak nature of the interaction of lipids with AQPZ (Laganowsky et al., 2014).

In vitro, AQP0 can be induced to form 2D crystals by choosing a very specific lipid-to-protein ratio (LPR) for reconstitution, but this *in-vitro* approach does not explain why AQP0 tetramers form 2D arrays in native lens membranes, which contain an excess of lipids as well as other membrane proteins. Since lipids mediate the interactions in AQP0 2D arrays, it is likely that specific lipids play a role in the assembly of AQP0 2D arrays in the native lens membrane. As AQP0-containing lens membrane junctions are greatly enriched in cholesterol and sphingomyelin (Fleschner and Cenedella, 1991), lipids that play a key role in raft formation (Brown and London, 2000), these lipids were prime candidates to drive AQP0 array formation. To gain structural insights into how cholesterol and/or sphingomyelin may induce AQP0 to form 2D crystals *in vivo* and potentially to obtain a more general understanding of how these lipids can establish lipid microdomains, we determined structures of AQP0 in membranes formed by mixtures of sphingomyelin and cholesterol and performed extensive equilibrium and force-probe MD simulations.

Results

AQP0 forms 2D crystals with all tested cholesterol/sphingomyelin mixtures

Purified AQP0 was reconstituted with mixtures of sphingomyelin and cholesterol at molar ratios of 1:0, 3:1, 2:1, 1:1, 1:2, 1:4 and 0:1 (Figure 1A–E). Every lipid mixture yielded membranes,

which had a sheet-like morphology at sphingomyelin:cholesterol ratios of up to 1:2 and formed vesicles at higher cholesterol percentages. In every case, power spectra of images taken of trehalose-embedded samples showed diffraction spots consistent with typical 2D arrays of AQP0 (data not shown).

Notably, even reconstitution of AQP0 with pure cholesterol yielded vesicles, which displayed a tendency to stack (Figure 1E). Cholesterol on its own does not form bilayers under physiological conditions and requires a molecule of complementary shape to do so (Kumar, 1991; Raguz et al., 2011). AQP0 appears to fulfill this requirement as it does form membranes with cholesterol. However, reconstitution of AQP0 with cholesterol only yielded membranes within a narrow LPR range, from 0.2 to 0.4. At higher or lower LPRs, only protein aggregates and no membranes were observed.

Fourier transforms of cryo-EM images of trehalose-embedded AQP0 2D crystals formed with cholesterol at an LPR of 0.4 showed clear reflections (Figure 1–figure supplement 2), establishing that the crystals have the same lattice constants as all other AQP0 2D crystals analyzed to date ($a = 65.5$ Å, $b = 65.5$ Å, and $\gamma = 90°$). Phase comparisons of the reflections showed that the crystals have $p422$ plane symmetry (Table 1) and thus have to be double-layered. Merging of 15 images yielded a projection map at 3.2-Å resolution (Figure 1F and Table 2). Although the crystals were not of sufficient quality to determine a high-resolution three-dimensional (3D) density map, the 2D projection map shows that AQP0 tetramers in a pure cholesterol membrane are organized in the same way as in membranes formed with all other lipids analyzed to date.

Structure determination of AQP0$_{2SM:1Chol}$

Fourier transforms of images of trehalose-embedded AQP0 crystals obtained with sphingomyelin/cholesterol mixtures showed reflections to a resolution of about 2 Å (Chiu et al., 2015). We focused first on AQP0 2D crystals obtained with a sphingomyelin/cholesterol mixture at a molar ratio of 2:1, from here on referred to as AQP0$_{2SM:1Chol}$. We collected electron diffraction patterns of these crystals at different tilt angles under low-dose conditions. While diffraction patterns recorded from untilted crystals showed reflections to a resolution of 2 Å (Figure 2A), reflections in diffraction patterns from highly tilted crystals were not visible beyond a resolution of 2.5 Å (Figure 2–figure supplement 1A).

After merging 214 diffraction patterns from crystals tilted up to ~72º and phasing the intensity dataset by molecular replacement, we were able to calculate a 3D density map at 2.5-Å resolution (Figure 2B), which made it possible to model the AQP0 structure. To build the sphingomyelin molecules, we initially only modeled the head groups and 10 carbon atoms for each of the two acyl chains. If the $2F_o$-F_c map after crystallographic refinement showed additional density, we extended the acyl chains, and this cycle was iterated. To avoid over-fitting, after each iteration, we assessed the values for R_{work}, R_{free} and their difference, as well as the consistency of the calculated $2F_o$-F_c map with the composite omit map. The final model includes seven sphingomyelin molecules, SM1 to SM7, with acyl chains ranging from 11 to 16 carbon atoms in length (Figure 3A). The one density in the map that was consistent with the characteristic four-ring structure of cholesterol was modeled as Chol1 (Figure 3A). The density in the center of four adjacent AQP0 tetramers around the four-fold symmetry axis was poorly resolved and could not be modeled (Figure 3–figure supplement 1B). The statistics for electron crystallographic data collection, model building, refinement and validation of AQP0$_{2SM:1Chol}$ are summarized in Table 3.

The structure of AQP0$_{2SM:1Chol}$ shows an AQP0 array with a low cholesterol content

AQP0 in the 2:1 sphingomyelin/cholesterol membrane adopts the same conformation as it does in a DMPC bilayer, AQP0$_{DMPC}$ (Gonen et al., 2005), and in an *E. coli* polar lipid extract (EPL) bilayer, AQP0$_{EPL}$ (Hite et al., 2010), with root mean square deviation (RMSD) between the Cα atoms of 0.271 Å and 0.264 Å, respectively (Figure 3–figure supplement 2A–B). The densities of the side chains along the water permeation pathway were clearly resolved as were the water molecules (Figure 2B). The water pathway through the AQP0 subunits showed density for four water molecules, at positions similar to those seen in previous electron crystallographic AQP0 structures (Gonen et al., 2004; Hite et al., 2010).

Comparison of the lipid bilayer in the AQP0$_{2SM:1Chol}$ structure (Figure 3A) with those in the AQP0$_{DMPC}$ and AQP0$_{EPL}$ structures (Figure 3B–C) shows that the seven sphingomyelin molecules assume similar positions as the DMPC and EPL lipids, further strengthening the earlier conclusion that annular lipids are not randomly distributed around a membrane protein but assume preferred positions (Hite et al., 2010). The density for sphingomyelin SM3 is well defined. The carbonyl oxygen of its head group is hydrogen-bonded with the tyrosyl side chain of Tyr105 and the amide oxygen of the guanidinium side chain of Arg196 (Figure 3–figure supplement 3A). However, the head groups of the remaining sphingomyelin lipids do not form specific interactions with AQP0, as reported for the DMPC and EPL head groups in the previous AQP0$_{DMPC}$ and AQP0$_{EPL}$ structures. Also, as observed in those structures, the sphingomyelin acyl chains follow grooves on the surface of AQP0.

The only cholesterol molecule, Chol1, resolved in the AQP0$_{2SM:1Chol}$ structure is located in the extracellular leaflet (Figure 3A). The tetracyclic ring of Chol1 makes π-stacking

interactions with AQP0 residues His201 and Trp205, and its alkyl tail makes van der Waals interactions with residues Ile87 and Val90 (Figure 3–figure supplement 3B). Chol1 also interacts extensively with the adjacent sphingolipid in the extracellular leaflet, SM2, the acyl chains of which assume an all *anti*-dihedral conformation, increasing their conformational order (Figure 3–figure supplement 3B).

While Chol1 may increase the conformational order of adjacent SM2, this effect is unlikely to induce AQP0 to form an array. Similarly, the location of Chol1 with respect to adjacent AQP0 tetramers (Figure 3–figure supplement 1B) does not provide any clues as to how it could affect array formation *in situ*. We therefore decided to analyze the structure of AQP0 in a membrane that has a higher cholesterol content.

Structure determination of AQP0$_{1SM:2Chol}$

Lens membranes contain more cholesterol than is represented by the AQP0$_{2SM:1Chol}$ structure. Therefore, we determined the structure of AQP0 2D crystals that were grown at a molar sphingomyelin:cholesterol ratio of 1:2, which is close to the lipid composition of human lens core membranes (Fleschner and Cenedella, 1991; Zelenka, 1984). These crystals were even better ordered, and electron diffraction patterns of untilted specimens showed reflections to a resolution better than 1.6 Å (Figure 2C). Diffraction patterns of 2D crystals tilted to 60° showed reflections to a resolution of ~2.5 Å (Figure 2–figure supplement 1B). We used the same data collection and processing scheme for AQP0$_{2SM:1Chol}$ to obtain a density map for AQP0$_{1SM:2Chol}$ at 2.5 Å resolution (Figure 2D). The density map allowed us to model AQP0, five sphingomyelin molecules, SM2, SM3, SM5, SM6 and SM7 (numbers corresponding to the sphingomyelin molecules in AQP0$_{2SM:1Chol}$) as well as four cholesterols (Figure 4A). As with the AQP0$_{1SM:2Chol}$

9

structure, it was not possible to model lipids in the area near the four-fold axis, where four AQP0 tetramers come together (Figure 3–figure supplement 1D). The statistics for the AQP0$_{1SM:2Chol}$ structure are summarized in Table 3.

The structure of AQP0$_{1SM:2Chol}$ shows an AQP0 array with a high cholesterol content

Superimposition of the AQP0$_{1SM:2Chol}$ structure with the AQP0$_{2SM:1Chol}$, AQP0$_{DMPC}$ and AQP0$_{EPL}$ structures yielded RMSD values between the Cα atoms of 0.431 Å, 0.390 Å and 0.362 Å (Figure 3–figure supplement 2C–E), again showing that the lipid environment has no detectable effect on the conformation of AQP0. Also, the water pathway in AQP0$_{1SM:2Chol}$ showed the same densities representing water molecules as observed in the AQP0$_{2SM:1Chol}$ structure. Hence, the AQP0 structure is essentially identical in the two analyzed sphingomyelin/cholesterol bilayers.

In the AQP0$_{2SM:1Chol}$ structure, an AQP0 subunit is surrounded by seven sphingomyelin molecules, but in the AQP0$_{1SM:2Chol}$ structure, due to the higher cholesterol content, two of the sphingomyelins in the extracellular leaflet, SM1 and SM4, have been replaced by cholesterols (Figure 4A–B). Of the two sphingomyelins remaining in the extracellular leaflet, the conformation of SM3 is virtually identical to that in the AQP0$_{2SM:1Chol}$ structure (Figure 4C). The other sphingomyelin in the extracellular leaflet, SM2, as well as the three sphingomyelins in the cytoplasmic leaflets, SM5 – SM7, all occupy similar positions as their counterparts in the AQP0$_{2SM:1Chol}$ structure, but adopt different conformations. In particular, SM2 and SM6 adapt their conformation to accommodate the additional cholesterol molecules. With the exception of SM3, the head group of which is stabilized by identical interactions with AQP0 in AQP0$_{2SM:1Chol}$ and AQP0$_{1SM:2Chol}$, the head groups of all other corresponding sphingomyelins are different in the

10

two structures (Figure 4C), corroborating the general lack of specific lipid–protein interactions in the head-group region.

The four cholesterol molecules in the $AQP0_{1SM:2Chol}$ structure show an interesting distribution. Overlaying the two bilayers shows that Chol1 in $AQP0_{1SM:2Chol}$ almost perfectly overlaps with Chol1 in $AQP0_{2SM:1Chol}$ (Figure 4C), and Chol1 interacts with AQP0 in the same way in the two structures, strengthening the notion that this is the preferred location for cholesterol to interact with AQP0. In the $AQP0_{2SM:1Chol}$ structure, Chol1 also interacts extensively with the adjacent sphingolipids, but some of these interactions are absent in the $AQP0_{1SM:2Chol}$ structure, due to the presence of the additional Chol2 (Figure 4A). The interaction with extracellular sphingomyelin SM1 in $AQP0_{2SM:1Chol}$ is replaced by an interaction with an acyl chain from cytoplasmic sphingomyelin SM5 (Figure 4C). Notably, however, despite their proximity, there do not seem to be any direct interactions between the two cholesterols (Figure 4–figure supplement 1A).

In addition to Chol1 and Chol2 in the extracellular leaflet, another cholesterol, Chol4, is located in the cytoplasmic leaflet (Figure 4A). Like Chol1 and Chol2, Chol4 interacts with AQP0 surface areas that feature aromatic residues (Figure 4D), in particular tryptophan and phenylalanine residues, which appear to make π-stacking interactions with the cholesterol ring system (Burley and Petsko, 1985; McGaughey et al., 1998) (Figure 4–figure supplement 1).

Chol3 is the most unusual cholesterol molecule seen in the $AQP0_{1SM:2Chol}$ structure. While all other cholesterols are either within the extracellular or cytoplasmic leaflet, Chol3 is located almost in the middle of the bilayer, with its hydroxyl head group located in the middle of the extracellular leaflet (Figure 4A–figure supplement 3). It sits in a pocket between the two adjacent AQP0 tetramers that is wider in the extracellular leaflet than the cytoplasmic leaflet

11

(Figure 4E). The orientation of Chol3 is that of the other cholesterols in the extracellular leaflet, suggesting that it originated from that leaflet. There are three phenylalanine residues in the vicinity of Chol3, but these do not form π-stacking interactions with its ring system but are close to its acyl chain (Figure 4E).

To assess the influence of cholesterol content on the hydrophobic thickness of the membrane, we measured the average distance between the phosphorus atoms of the phosphodiester groups and the nitrogen atoms of the amide groups of the sphingomyelins in the two leaflets (Figure 1–figure supplement 1), which were 36.8 Å and 31.3 Å, respectively, for the AQP01SM:2Chol bilayer (Figure 4A) and 33.9 Å and 27.1 Å, respectively, for the AQP02SM:1Chol bilayer (Figure 4B).

Cholesterol positions observed in the electron crystallographic structures are representative of those around single AQP0 tetramers

The electron crystallographic structures of AQP0 were obtained with 2D crystals, in which the lipids are constrained by the packing of the AQP0 tetramers. Therefore, we performed MD simulations and calculated time-averaged densities to investigate if the cholesterol positions seen in these structures represent the positions unconstrained cholesterol would adopt around individual AQP0 tetramers, as has previously been shown to be the case for DMPC lipids (Aponte-Santamaría et al., 2012). The electron crystallographic AQP0 structures obtained with SM:Chol ratios of 2:1, AQP0$_{2SM:1Chol}$, and 1:2, AQP0$_{1SM:2Chol}$, revealed distinct localization patterns for cholesterol around AQP0. In the AQP0$_{2SM:1Chol}$ structure, a single cholesterol molecule was observed, associated with AQP0 surface S1 (Figure 5, top). This cholesterol position was also identified in a previous MD simulation study (O'Connor and Klauda, 2011). In

the density map representing the average localization of cholesterol around AQP0 over time that we calculated from MD simulations of an individual AQP0 tetramer in a 2:1 SM:Chol membrane (Figure 5–figure supplement 1B), we also found a high cholesterol density in the same position (Figure 5, top). The simulations identified an additional hotspot, located on the extracellular side of surface S1 (see high density marked with an asterisk in Figure 5, top). No cholesterol was observed in this position in the AQP0$_{2SM:1Chol}$ structure, suggesting that it may be preferentially occupied by cholesterol around single AQP0 tetramers but may be unfavorable in the context of AQP0 arrays. In contrast, the AQP0$_{1SM:2Chol}$ structure revealed four cholesterol molecules associated with the AQP0 surface (Figure 5, bottom), including the one seen at the SM:Chol ratio of 2:1. Our simulations at that high cholesterol concentration largely recapitulated these positions, as seen by the high cholesterol densities at positions for Chol1, Chol2, Chol3, and Chol4 (Figure 5, bottom).

A particularly interesting cholesterol in the AQP0$_{1SM:2Chol}$ structure is Chol3, which is localized close to the center of the lipid bilayer and is therefore referred to as "deep cholesterol". Our density map representing the average cholesterol localization over time calculated for the high cholesterol concentration shows high density close to the position of Chol3, on both surfaces S1 and S2, but this density is localized to the extracellular leaflet rather than the middle of the membrane (Figure 5). This finding suggests that the deep cholesterol is not stable when cholesterol associates with individual AQP0 tetramers.

Thus, our simulations demonstrate, as previously shown for DMPC lipids (Aponte-Santamaría et al., 2012), that the crystalline packing of AQP0 tetramers in 2D crystals does, in general, not affect the positions where cholesterol preferentially interacts with AQP0. However, notably, deep-binding Chol3 seen in the AQP0$_{1SM:2Chol}$ structure is not represented in the MD

13

simulations using an isolated AQP0 tetramer. Therefore, we performed further simulations with pairs of AQP0 tetramers to assess whether the deep position of Chol3 represents a crystallographic artifact or may be the result of interface properties between two neighboring AQP0 tetramers.

Deep-binding cholesterol occurs at the interface between two AQP0 tetramers

To assess the behavior of the deep cholesterol associated with AQP0 in terms of orientation and membrane insertion depth (Figure 6A), we analyzed several different situations (Figure 6C-E). For this analysis, we initially positioned a cholesterol molecule in the middle of the bilayer according to the relative observed position of the deep cholesterol (Chol3) in the $AQP0_{1SM:2Chol}$ structure. For reference, we also simulated a cholesterol inserted at the equivalent position into a pure lipid membrane (Figure 6B). The presence of cholesterol in the membrane did not significantly alter the insertion depth of the monitored cholesterol. Within a few ns, cholesterol moved away from the deeply inserted position and equilibrated to a stable position with an insertion level of -0.73±0.31 nm (avg. ± s.d.) in a pure SM bilayer and -0.58±0.16 nm (avg. ± s.d.) and -0.60±0.16 nm in the 2:1 and 1:2 SM:Chol membranes, respectively (Figure 6B and Figure 6–figure supplement 1). In terms of orientation, an increasing cholesterol concentration in the membrane resulted in a decreasing tilt of the monitored cholesterol as well as in a narrower distribution (Figure 6B).

The behavior of the monitored deep cholesterol was very different when it was associated with AQP0. In this case, the protein becomes the main factor that defines its insertion depth and orientation (Figure 6C-D). The absence or presence of cholesterol in the membrane has no effect on the behavior of the AQP0-associated deep cholesterol: this sterol moved very quickly away

14

from the initial position (Figure 6–figure supplement 1) and stabilized at around -0.6 nm which is a similar value to that seen in SM membranes without AQP0 but less than that of the deep cholesterol seen in the AQP0$_{1SM:2Chol}$ structure where it is close to -1.0 nm (Figure 6C-D). In terms of orientation, the AQP0-associated deep cholesterol sampled tilt angles up to ~70° with a distribution rather insensitive to the cholesterol concentration in the membrane (Fig 6C-D). Moreover, it appears that both surfaces of AQP0, S1 and S2, have a similar effect on the insertion depth and orientation of the associated deep cholesterol (compare Figure 6C and 6D).

The behavior of the deep cholesterol changed again when it was sandwiched in between two neighboring AQP0 tetramers. While the tilt distribution of the cholesterol is comparable to when it interacts only with one AQP0 tetramer, although it may be able to adopt slightly larger tilts, the insertion depth is distinctly different (Figure 6E). Here the average insertion depth of -1.16±0.50 nm is now similar to the position of Chol3 in the AQP0$_{1SM:2Chol}$ structure of -1.0 nm.

Note that we observed a few spontaneous cholesterol flip-flop events, as previously observed in other microsecond-scale simulations (Gu et al., 2019; Jo et al., 2010; Marino et al., 2016), resulting in this particular case in the small peaks at ~-3.25 nm insertion and ~135° orientation in Figure 6E (see also the sudden drop in the insertion time trace in Figure 6–figure supplement 1).

In summary, our simulations show that the association of a cholesterol with an individual AQP0 tetramer defines the extent of its insertion depth and orientation, overriding any effect that the cholesterol concentration of the surrounding membrane may have. Furthermore, the association of a cholesterol with two adjacent AQP0 tetramers induces it to localize much deeper in the membrane than otherwise observed and supports the position of Chol3 seen in the AQP0$_{1SM:2Chol}$ structure.

Sandwiched cholesterol increases the force needed to separate adjacent AQP0 tetramers

Considering the different behavior of cholesterol associated with one AQP0 tetramer *versus* being sandwiched in between two adjacent tetramers, we next asked whether the presence of cholesterol in between two AQP0 tetramers could have an effect on the stability of their association. We considered two lipid interfaces between the two neighboring tetramers: an "SM interface" that consisted of only SM lipids at the positions seen in the $AQP0_{2SM:1Chol}$ structure, and a second identical one, except that two SM molecules were replaced by the deep-binding Chol3 molecules in the position observed in the $AQP0_{1SM:2Chol}$ structure (Figure 5–figure supplement 1D). Comparison of these two cases should allow us to assess the effect of the deep-binding Chol3 molecules on the mechanical stability of the associated AQP0 tetramers. During a cumulative time of 10 μs of equilibrium MD simulations, the two AQP0 tetramers overall behaved very similarly for the two interfaces and stayed close together (Figure 7A), exhibiting only minor variations (of less than 13.4°) in angular lateral, tilt and torsional intra-tetramer motions (Figure 7B). To explore the effect of the deep cholesterols on the mechanical stability of the paired tetramers in response to a lateral mechanical perturbation, we applied an external harmonic force to the tetramers, attaching virtual springs to their centers of mass and moving these springs in opposite directions at constant velocity (Figure 7C). The force exerted on the two tetramers was ramped up until the two tetramers detached from each other and the force leveled off (Figure 7D-E). The resulting force-distance profiles revealed that the tetramer pairs withstood a higher force before detachment when cholesterol was present at the interface (Figure 7E-F). More quantitatively, at our fastest pulling rate of 0.1 m/s, at which the integrity of the membrane was still maintained, the detachment forces were not significantly different whether

the interface contained cholesterol or not (Figure 7F). However, for the slower pulling rates of 0.02 m/s and 0.004 m/s, which are more relevant, because there should not be strong forces pulling on AQP0 tetramers in native membranes, the detachment force required to separate the tetramers was statistically significantly higher when their interface contained cholesterol (Figure 7F). Thus, because a higher force is required to separate neighboring AQP0 tetramers when cholesterol is present at their interface, deep cholesterols appear to mechanically stabilize AQP0 arrays.

Protein–protein interactions affect the stability of associated AQP0 tetramers

We performed a further analysis in an effort to understand why the presence of cholesterol at the interface would increase the force needed to separate associated AQP0 tetramers. For this purpose, we calculated density maps representing what components the surface of an AQP0 tetramer interacts with over time. In the absence of cholesterol, the AQP0 surface is completely covered by sphingomyelin in the hydrophobic region of the membrane and by water outside this region (Figure 8A, left column). As noted before, there are essentially no direct protein–protein interactions between the adjacent tetramers. When cholesterol was present at the interface, it interacted with AQP0 at the center of the membrane and remained mostly in place (Figure 8A, right column). While the area below the cholesterols towards the cytoplasmic surface is occupied by sphingomyelin as in the interface lacking cholesterol, the area above the cholesterols towards the extracellular surface is now covered with water (Figure 8A, left column), which is in close proximity to the cholesterol oxygen group (Figure 8–figure supplement 1), and now also forms direct protein–protein interactions with the adjacent tetramer (Figure 8A, left column, and Figure 8–figure supplement 2). We further analyzed these interactions, by computing the overall

17

fraction of time during which residue–residue contacts formed (Figure 8B-C) and their average lifetimes (Figure 8D). The overall fraction is a thermodynamic quantity that relates to the probability of formation of these contacts, while the lifetime is related to the kinetics of this process. The probability of formation increased mainly for residue pairs above the two cholesterol molecules (Figure 8B-C). The lifetime also slightly increased for the residue pairs above the cholesterol molecules, but these contacts occurred mainly among the highly flexible amino acid side-chains and were short-lived, i.e., smaller than 1 ns (Figure 8D).

Only one inter-tetramer contact was observed in the electron crystallographic structure of AQP0 in a high cholesterol membrane, $AQP0_{1SM:2Chol}$, namely $Leu217_{Tet1}$-$Phe14_{Tet12}$. This contact was also observed in our simulations (Figure 8B–D). However, the $AQP0_{1SM:2Chol}$ structure did not reveal protein–protein contacts above the cholesterol molecules (Figure 8B–D). A possible explanation for this discrepancy is that although such contacts could be observed in our simulations for the cholesterol-containing interface, they had a rather low probability to occur (only up to 20% of the simulated time, Figure 8C). Thus, the electron crystallographic structure would visualize other contacts with a higher probability, in particular protein–water interactions (Figure 8A, left column).

Lipid–protein surface complementarity may also enhance mechanical resistance of associated AQP0 tetramers

We found that the presence of cholesterol at the interface results in new protein–protein interactions between adjacent AQP0 tetramers that may increase the stability of their association, but we wondered whether the cholesterol itself could contribute to the increased force needed to separate associated tetramers. Surface complementarity has previously been suggested to play a

18

key role in modulating lipid–protein interactions (Aponte-Santamaría et al., 2012; Niemelä et al., 2010) with particular relevance for cholesterol (Kurth et al., 2020), prompting us to analyze the surface complementarity between AQP0 and cholesterol. We quantified surface complementarity as the contact area between the sandwiched lipids (either cholesterol or sphingomyelin) and the two tetramers, $A_{Contact}$, and normalized it by the surface area of the lipid in question, A_{Lipid}, i.e., a larger $A_{Contact}/A_{Lipid}$ ratio would indicate a higher surface complementarity between the lipid and the proteins (see Methods for details of this calculation and Figure 8E for a schematic diagram). We calculated the $A_{Contact}/A_{Lipid}$ ratio from the equilibrium simulations. Remarkably, the sandwiched cholesterol displayed a higher surface complementarity than the sandwiched sphingomyelin (Figure 8F). This analysis thus suggests that cholesterol better accommodates to the roughness of the two AQP0 tetramer surfaces than sphingomyelin can, a feature that may contribute to the enhanced resistance of associated tetramers to detach when cholesterol is present at their interface.

Discussion

In this study, we determined two electron crystallographic structures of AQP0 in membranes formed by sphingomyelin and cholesterol. As these so-called raft lipids are the main constituents of lens membranes, they represent the natural environment of AQP0. The AQP0 crystals formed in sphingomyelin/cholesterol membranes have the same lattice constants as previous 2D crystals obtained with other lipids (Gonen et al., 2005; Hite et al., 2010) as well as the 2D arrays found in lens membranes (Buzhynskyy et al., 2007). The 2D crystals thus reflect the arrangement of AQP0 tetramers in native 2D arrays.

Our structure of AQP0$_{2SM:1Chol}$ reveals seven sphingomyelins (Figure 3A), the same number of lipids also seen in structures of AQP0 in bilayers formed by DMPC (Gonen et al., 2005) and EPL (Hite et al., 2010), and these are also located in almost identical positions (Figure 3B–C). The interaction of sphingomyelins with AQP0 thus seem to be governed by the same principles that were found for phosphoglycerolipids, namely that the acyl chains locate to grooves in the protein surface and that the lipid head groups make few if any interactions with the protein (Hite et al., 2010). However, compared to the acyl chains in the EPL bilayer, those of the sphingomyelins appear to be straighter, which likely reflects the saturated nature of the sphingomyelin acyl chains. Despite this difference, the structure of the sphingomyelin bilayer is very similar to those of bilayers formed by phosphoglycerolipids, indicating that sphingomyelin by itself is unlikely the reason for AQP0 to form 2D arrays in lens membranes.

Cholesterol has a higher affinity for sphingomyelin than for phosphoglycerolipids (Niu and Litman, 2002), because the mostly saturated acyl chains of sphingomyelin can better accommodate the planar ring system of cholesterol (Epand and Epand, 2004; Zheng et al., 2007) and because the sphingomyelin backbone has two hydrogen-bond donor groups, an amide and a hydroxyl group, that make hydrogen bonding to cholesterol more effective (Róg and Pasenkiewicz-Gierula, 2006). Furthermore, the interaction of the sphingomyelin amide group with the hydroxyl group of cholesterol orients the smooth (α) face of the cholesterol towards sphingomyelin, leaving only the rough (β) face to interact with membrane proteins (Fantini and Barrantes, 2013). In the context of AQP0 2D arrays, however, these interactions do not appear to occur. While Chol1 does interact with sphingomyelin acyl chains in both structures, the additional cholesterols in the AQP0$_{1SM:2Chol}$ structure seem to have little interactions with sphingomyelin acyl chains and instead seem to substitute for some of the sphingomyelin acyl

chains seen in the AQP0$_{2SM:1Chol}$ structure (Figure 4A and C). We also do not observe interactions between the hydroxyl head group of any cholesterols with an amide group of the sphingomyelins. While we cannot rule out that specific sphingomyelin–cholesterol interactions occur in the membrane area enclosed by four AQP0 tetramers (where we were unable to build models for the lipids due to the four-fold symmetry axis), our structures suggest that specific sphingomyelin–cholesterol interactions do not play a critical role in AQP0 array formation in the lens membrane.

Cholesterol increases the order of lipid acyl chains (de Meyer and Smit, 2009; Lafleur et al., 1990), and the resulting phase transition is thought to contribute to the segregation of cholesterol-enriched membrane areas (Pandit et al., 2007). A potential mechanism by which cholesterol could induce AQP0 array formation could thus be that cholesterol bound to AQP0 would order the surrounding lipids, leading to a phase transition that leads to an initial segregation and crystallization of the AQP0/cholesterol/sphingomyelin units in the membrane.

In an attempt to assess this possibility, we looked at the B-factors of the acyl chains, which are affected, among other factors, by the mobility of the atoms. Comparison of corresponding acyl chains showed that the B-factors of the acyl chains in the AQP0$_{1SM:2Chol}$ structure tend to be slightly lower than those of the acyl chains in the AQP0$_{2SM:1Chol}$ structure (Figure 4–figure supplement 2), suggesting that the cholesterols could have an ordering effect on the sphingomyelin acyl chains. However, the B-factors of the acyl chains in the AQP0$_{EPL}$ structure, which contain double bonds and are not constrained by cholesterol and should thus be much less ordered, are similar to those of the acyl chains in the AQP0$_{2SM:1Chol}$ structure. A likely explanation is that acyl chains, including unsaturated ones, preferentially fill in grooves in the protein surface (Hite et al., 2010), which should already substantially constrain their mobility.

21

Therefore, cholesterol bound to the protein surface may not add much additional constraints to their already restricted mobility. Cholesterol-induced phase separation thus does not seem to be a likely cause for AQP0 array formation.

The hydrophobic thickness is an important characteristic of a lipid bilayer, which depends on the length and saturation of the acyl chains of the lipids forming the bilayer. Mismatch of the hydrophobic thickness between a membrane protein and the lipid bilayer is thought to be one mechanism by which membrane proteins can cluster in a membrane (Hanulová and Weiss, 2012; Schmidt et al., 2008). One factor that affects the hydrophobic thickness of a membrane is its cholesterol content, which is related to the ordering effect of cholesterol on the lipid acyl chains (de Meyer and Smit, 2009; Lafleur et al., 1990). Change in cholesterol-induced hydrophobic thickness may thus be another potential force that drives the formation of AQP0 arrays in the lens membrane. Our measurements of the average distance between the phosphorus atoms of the phosphodiester groups and the nitrogen atoms of the amide groups of the sphingomyelins in the two leaflets (Figure 4A–B) show that both distances are larger for the bilayer with the higher cholesterol content, by ~3 Å for the phosphodiester groups and ~4 Å for the amide groups, suggesting that a higher cholesterol content indeed increases the hydrophobic thickness of the bilayer formed by the annular sphingomyelins.

In cells, sphingomyelin is predominantly found in the extracellular leaflet of the plasma membrane (Devaux, 1991), so that sphingomyelins seen in the extracellular leaflet in our two structures likely represent true positions of sphingomyelin in native AQP0 2D arrays. The two sphingomyelins in the extracellular leaflet that are seen in both sphingomyelin/cholesterol membranes are in exactly the same position (Figure 4C), establishing that the extracellular leaflet does not change its position relative to AQP0 upon thickening of the membrane with increasing

cholesterol content. Sphingomyelin SM3 may be responsible for the fixed position of the extracellular leaflet. In all structures of AQP0 in different lipid bilayers, the lipid at the position equivalent to that of SM3 always has the best-defined density and the lowest B-factors (including for the acyl chains; Figure 4–figure supplement 2). The lipid at this position is always the only one whose head group makes interactions with AQP0. It is thus possible that the lipid at this position defines and locks in the position of the extracellular leaflet with respect to AQP0. As a result, the extracellular leaflet does not play a role in defining the thickness of the membrane.

The increase in hydrophobic thickness with higher cholesterol content is the result of the three sphingomyelins in the cytoplasmic leaflet moving further out from the bilayer center, which they do even though this leaflet contains only a single cholesterol (Figure 4C). The notion that an increase in hydrophobic thickness is predominantly due to movements of lipids in the cytoplasmic leaflet is consistent with the observation that these lipids are usually more mobile, i.e., have higher B-factors in crystal structure than lipids in the extracellular leaflet (Belrhali et al., 1999). Comparison of the lipid arrangement in the cytoplasmic leaflet shows that Chol4 in the AQP0$_{1SM:2Chol}$ structure assumes the position of SM6 in the AQP0$_{2SM:1Chol}$ structure (Figure 4A–C). The new position of the displaced SM6 in the AQP0$_{1SM:2Chol}$ structure is further out from the bilayer center and potentially is the cause for similar outward movements of lipids SM5 and SM7, thus defining the new position of the cytoplasmic leaflet and increasing the hydrophobic thickness of the annular lipid bilayer. Hence, a higher cholesterol concentration of the membrane does increase the hydrophobic thickness of the lipid bilayer formed by the annular lipids surrounding AQP0 tetramers, thus creating a hydrophobic mismatch with the remaining lipid bilayer, which, in turn, would provide a driving force for AQP0 tetramers to cluster in the native lens membrane.

The cholesterols in our structures do not interact with AQP0 through consensus cholesterol-binding sites known as the Cholesterol Recognition/interaction Aminoacid Consensus sequence (CRAC domain; -L/V-$(X)_{1-5}$-Y-$(X)_{1-5}$-R/K-) (Li and Papadopoulos, 1998) or the inverted CRAC domain, CARC (Baier et al., 2011). Cholesterol can also bind to membrane proteins in a fashion that does not involve a CRAC or CARC domain, as seen for example for the influenza M2 protein (Elkins et al., 2018, 2017) and α-synuclein (Fantini et al., 2011). Emerging cryo-EM structures of G protein-coupled receptors (GPCRs) also do not show a consensus motif for their interaction with cholesterol (Sarkar and Chattopadhyay, 2020; Taghon et al., 2021). Furthermore, the cholesterols interact with AQP0 through their smooth α face (Figure 4–figure supplement 1), which is not engaged in interactions with sphingomyelin as previously thought (Fantini and Barrantes, 2013), thus differing from the predominant interaction of cholesterols with GPCRs, the G-protein-gated inwardly rectifying potassium-2 (GIRK2) channel, and the Na^+, K^+-ATPase, which occur predominantly through the rough β face of cholesterol (Gimpl, 2016; Mathiharan et al., 2021; Shinoda et al., 2009). However, there are other cases in which cholesterol interacts with membrane proteins through its α face, such as seen for the Niemann-Pick C1-like 1 protein (Huang et al., 2020). Likely the residues on the protein surface determine whether a protein interacts with cholesterol through its α or β face. The smooth α face interacts with aromatic side chains through π-stacking (Nishio et al., 1995), whereas the β face appears to interact with hydrophobic side chains, such as leucine, valine, or isoleucine (Fantini et al., 2011).

Chol3 is the most unusual lipid in our structures, because it is located in the middle of the lipid bilayer and because it is sandwiched between two neighboring AQP tetramers. Binding sites for cholesterol in the middle of the membrane have also been described for GPCRs, and

these sites have been named "deep binding sites" (Genheden et al., 2017). A docking

investigation with known membrane protein structures for cholesterol-binding sites revealed

deep binding sites not only in GPCRs but also in ion channels and transporters (Lee, 2018).

Unlike any other cholesterol in our structures, Chol3 interacts directly with two AQP0 subunits

that are part of different tetramers. This interaction is different from the cholesterol-induced

dimerization of GPCRs as these are mediated by interactions between two or more cholesterol

molecules rather than one cholesterol directly interacting with two GPCRs (Gimpl, 2016;

Hanson et al., 2008). The two adjacent AQP0 tetramers form a pocket that is ~8.5 Å wide at the

position of the ring system and ~2.5 Å at the position of the acyl chain (Figure 4E). The

interaction surface on the AQP0 subunit interacting with the smooth face of Chol3 encompasses

373 Å^2 and is formed by residues Ser106, Val103, Ala102, Ala99, and Leu21, which line the

ring system, and three phenylalanine residues, Phe17, Phe18 and Phe14, which surround the acyl

chain. The interaction surface on the AQP0 subunit interacting with the rough face of Chol3 is

344 Å^2 and is predominantly formed by residues Ile132, Ile135, Phe136, Ile210, Leu214, and

Leu217 (Figure 4E). Leucine and isoleucine residues have also been found to mediate the

interaction of many GPCRs with the rough β face of cholesterol (Gimpl, 2016). The hydroxyl

head group of Chol3 interacts with a water molecule that may be stabilized through an

interaction with Ser126 (Figure 4E). Because of its intricate interactions with two AQP0

subunits, Chol3 can likely function as a glue that can keep two tetramers together. This structural

characteristic may be the reason why AQP0 can form 2D arrays in pure cholesterol membranes

(Figure 1E and 1F).

To gain further insights into the role cholesterol plays in the stability of AQP0 arrays, we

used MD simulations to investigate the interplay between cholesterol and AQP0. The first set of

25

simulations investigated the localization of cholesterol around a single AQP0 tetramer. Cholesterol positioned at well-defined positions, i.e., hotspots, that were in notable agreement with both the predicted positions from a previous computational study (O'Connor and Klauda, 2011) as well as the positions in the electron crystallographic structures (Figure 5). Therefore, as it has been previously demonstrated to be the case for phospholipids (Aponte-Santamaría et al., 2012), the crystal packing in the crystallographic structures does not greatly affect the positioning of cholesterol around AQP0. In consequence, crystallographic cholesterol positions recapitulate the behavior of unconstrained cholesterol molecules around a single AQP0 tetramer. This is the case for all cholesterols except for one, the deep cholesterol, which will be discussed in detail below. Cholesterol localization around membrane proteins has been extensively studied, especially in the context of the regulation and activity of G protein-coupled receptors (GPCRs), exchangers and ion channels, but also aquaporins (for a comprehensive review see (Corradi et al., 2019)). Interestingly, in coarse-grained MD simulations, when AQP1 was embedded in a lipid bilayer resembling the plasma membrane, cholesterol was enriched at two positions that qualitatively correspond to the lateral projections of Chol3 and Chol4 positions observed here for AQP0 (compare Figure 5 with Figure 2 of (Corradi et al., 2018)). This suggests that individual AQP0 and AQP1 tetramers share similarities in their cholesterol-binding fingerprints, as was already shown for phospholipids in this protein family (Stansfeld et al., 2013). Nevertheless, cholesterol was rather depleted from the Chol1 position in AQP1. The shape of the protein surface has been shown to critically define the positions where lipids non-specifically associate with AQP0 (Aponte-Santamaría et al., 2012; Briones et al., 2017) and also other proteins (e.g., ion channels (Niemelä et al., 2010) and GPCRs (Kurth et al., 2020), among many others reviewed in (Corradi et al., 2019)). This principle presumably applies here, too, i.e., the different

surface of AQP0 at the Chol1 position, compared to that of AQP1, may result in a greater association of cholesterol over sphingolipids in this position (Figure 8–figure supplement 1).

In a second set of simulations, we attempted to understand the molecular reasons for the unusual position of deep binding Chol3 (Figure 6). We demonstrate that neither a single AQP0 tetramer (Figure 6C–D) nor a specific bulk cholesterol concentration (Figure 6B) is sufficient to maintain annular cholesterol molecules at such a deeply-inserted position. Instead, the constraint imposed by two adjacent AQP0 tetramers and the coordination of two water molecules were required (Figures 6E, 8A and Figure 8–figure supplement 1). Our data are thus consistent with the existence of deep cholesterol positions but only in a highly constrained setup that involves two AQP0 tetramers. The immediate questions raised by the existence of deep cholesterols are whether these affect the formation and/or stability of 2D AQP0 arrays.

Our simulations provide strong evidence for a direct influence of deep cholesterol molecules on the mechanical stability of the association between two adjacent AQP0 tetramers. We demonstrate that two adjacent tetramers can withstand larger lateral detachment forces when their interface contains deep cholesterol molecules (Figure 7C–F). Crystal structures of several membrane proteins already revealed that cholesterol can mediate crystal packing interactions (Crnjar and Molteni, 2021; Khunweeraphong et al., 2020; Wu et al., 2014). Moreover, the presence of cholesterol has been reported to influence membrane-protein oligomerization, a feature mainly explored for GPCRs (Corradi et al., 2019; Gahbauer and Böckmann, 2016). We expand on these data, by providing evidence of cholesterol—directly—engaging in the stronger attachment of two membrane proteins. We attribute this to cholesterol facilitating the formation of transient protein–protein contacts (Figure 8A–D) together with providing higher surface complementarity when sandwiched between two AQP0 tetramers (Figure 8E–F). Cardiolipin is a

phospholipid that has been implicated in stabilizing transient α-helical membrane protein oligomers (Gupta et al., 2017). More specifically, cardiolipin has been described to serve as a "glue" for the cytochrome components of the respiratory chain in mitochondrial membranes (Arnarez et al., 2013; Zhang et al., 2002). Interestingly, cardiolipin also impacts the resistance of AQPZ, the bacterial homolog of AQP0, to unfolding (Laganowsky et al., 2014). In addition, lipids have been recently shown to mediate protein assembly in the outer membrane of bacteria (Webby et al., 2022). Analogous to these systems and based on our electron crystallography structures and MD simulations, we propose that deep cholesterol increases the mechanical stability of associated AQP0 tetramers. Although we provide solid evidence here that deep cholesterol imparts mechanical stabilization, free energy calculations would be required to obtain the full picture of thermodynamic stabilization. However, such free energy calculations are challenging for lipids, due to the chemical complexity and poor convergence involved (Wang et al., 2021), and are thus beyond the scope of the current work.

Our structures of AQP0 arrays in sphingomyelin bilayers with low and high cholesterol content and the results from the MD simulations allow us to propose a model for cholesterol-induced array formation (Figure 9). In a lipid bilayer with a low cholesterol concentration, cholesterol may interact with AQP0 predominantly through the most specific cholesterol-binding site, the one occupied by Chol1, but this interaction would be transient and would not have a meaningful effect on the organization of the surrounding lipid molecules (sphingomyelin in our AQP0$_{2SM:1Chol}$ structure) (Figure 9A). An increase in cholesterol concentration will cause more cholesterols in the extracellular leaflet to bind to AQP0. In addition, cholesterol will also enrich in the cytoplasmic leaflet and associate with AQP0. This interaction will shift the annular lipids in this leaflet further away from the membrane center and create a hydrophobic mismatch

between the shell of annular lipids and the surrounding lipid bilayer (Figure 9B). Driven by the force to minimize membrane tension induced by hydrophobic mismatch, AQP0 tetramers will cluster. Cholesterols in between the tetramers can diffuse deeper into the membrane and associate with deep binding sites on AQP0, thus stabilizing the interaction between adjacent tetramers (Figure 9C). Alternatively, it may also be possible that cholesterol first interacts with a deep binding site on one AQP0 but is only stabilized as the second AQP0 traps it in position. As each AQP0 tetramer has four deep cholesterol-binding sites, the avidity effect would result in the formation and stabilization of large 2D arrays as those seen in native lens membranes (Figure 9D).

This model is specific for the formation of AQP0 arrays in lens membranes, but we speculate that similar principles may underlie the organization of lipid rafts. AQP0 may be special in that it forms tetramers and thus has four deep cholesterol-binding sites, so that the avidity effect allows it to form much larger domains than seen for typical lipid rafts (Simons and Ikonen, 1997; Zelenka, 1984). In addition, it is presumably not common that the same protein has surfaces that can interact with both the smooth α and the rough β face of cholesterol. However, cholesterol would have the potential to mediate the association of any protein with an α face-interacting surface with any other protein that features a β face-interacting surface. Thus, while hydrophobic mismatch and phase separation may be driving forces that bring proteins into close proximity, cholesterol may be the actual glue that increases the time they remain associated.

Materials and methods

Purification of AQP0

AQP0 was purified as described in Gonen et al. (2004). Briefly, dissected cores of sheep lenses (Wolverine Packing Company, Detroit, MI) were homogenized, and isolated membranes were sequentially washed with 10 mM Tris-HCl, pH 8.0, 4 M urea, and 20 mM NaOH, and then solubilized with 4% n-octyl-β-D-glucopyranoside (OG; Anatrace). Solubilized AQP0 was purified using anion-exchange (MonoQ; GE Healthcare) and size-exclusion (Superose-6; GE Healthcare) chromatography.

2D crystallization of AQP0

Purified AQP0 in 1.2% OG, 10 mM Tris-HCl (pH 8.0), and 100 mM NaCl was mixed at a lipid-to-protein ratio (LPR) (w/w) of 0.2 with different mixtures of OG-solubilized sphingomyelin (N-palmitoyl-D-erythro-sphingosylphosphorylcholine) (Avanti) and cholesterol (Avanti). The mixtures were placed into dialysis buttons, and the detergent was removed by dialysis at 37°C against 10 mM MES (pH 6.0), 300 mM NaCl, 30 mM $MgCl_2$, and 0.05% NaN_3 for one week with daily buffer exchanges. The 2D crystal samples were prepared by negative staining with uranyl formate and assessed on a Philips CM10 electron microscope.

Imaging and image processing of AQP0 2D crystals grown with pure cholesterol

$AQP0_{Chol}$ 2D crystals were prepared on molybdenum grids using the carbon sandwich method (Gyobu et al., 2004) and a trehalose concentration ranging from 3% to 5% (w/v). After blotting away excess trehalose solution with a filter paper, grids were quick-frozen in liquid nitrogen and transferred onto a cryo-specimen stage for EM data collection.

Data of untilted 2D crystals were collected with a Polara electron microscope (FEI Company, Hillsboro, OR) operated at an acceleration voltage of 300 kV and equipped with a Gatan K2 Summit direct electron detector camera (Gatan, Pleasanton, CA), using low-dose procedures, a calibrated magnification of 50,926x, and a defocus ranging from -500 to -1500 nm. Dose-fractionated images were recorded in super-resolution mode at a counting rate of 8 counts/pixel/sec (8.33 counts/Å^2/sec). Frames were read out every 150 ms and 16 frames were collected, resulting in an exposure time of 2.4 seconds and a total dose of 20 e^-/Å^2. Motion-corrected sum images were generated using the program MotionCorr (Li et al., 2013).

Images of AQP0$_{Chol}$ were computationally unbent and corrected for the effects of the contrast transfer function using the 2dx software (Gipson et al., 2007b). The plane group symmetry of the projection map was analyzed with ALLSPACE (Table 1) (Valpuesta et al., 1994). Fifteen images were merged using 2dx_merge (Gipson et al., 2007a), resulting in a projection map at 3.2 Å resolution. The phase residuals are listed in Table 2.

Collection of electron diffraction data

2D crystals grown at molar sphingomyelin:cholesterol ratios of 1:2 and 2:1 were prepared by trehalose embedding as described above.

Electron diffraction patterns of AQP0 2D crystals were recorded with a Polara electron microscope (FEI Company, Hillsboro, OR) operated at an acceleration voltage of 300 kV and equipped with a 4k ✕ 4k CCD camera (Gatan, Pleasanton, CA). The camera length was set to 1.9 m and a C2 aperture with a diameter of 30 μm was selected. The selected target areas on the grids were exposed for 30 seconds, corresponding to a total electron dose of approximately 10

electrons/$Å^2$. Diffraction patterns were collected at tilt angles of 0°, 20°, 45°, 60°, 65°, and 70°, and details are provided in Table 3.

Diffraction data processing and model building

The graphical user interface of the IPLT diffraction processing software was used to index electron diffraction patterns (Schenk et al., 2013). Diffraction patterns that showed multiple 2D lattices were discarded. After subtracting the background resulting from inelastic scattering, the intensities of the reflections were extracted, integrated according to their 2D Miller indices, and then merged into reciprocal lattice lines as described before (Gonen et al., 2004). The reconstructed 3D lattice lines were then iteratively refined against the experimental data enforcing a *p*422 plane symmetry. The refined lattice lines were sampled along the *z** direction using the "truncate" program in the CCP4 software package (Winn et al., 2011), assuming a crystal thickness of 200 Å. The dataset was phased by molecular replacement in PHASER (version 2.1) (McCoy et al., 2007), using as search template the AQP0$_{DMPC}$ structure (PDB code: 2B6O) but without the loops and C-terminal domain of AQP0 and without the DMPC lipids. The density map obtained with data recorded from AQP0 2D crystals formed with a molar sphingomyelin:cholesterol ratio of 2:1 allowed building of AQP0 residues Ser6 to Pro225 as well as seven sphingomyelins and one cholesterol. For the density map obtained with AQP0 crystals formed with a sphingomyelin:cholesterol ratio of 1:2, AQP0 could also be built from Ser6 to Pro225, and five sphingomyelin and four cholesterol molecules could be built. Models were built in Coot (version 0.8.2) (Emsley and Cowtan, 2004), and the topologies and geometry restraint parameters for cholesterol and sphingomyelin were generated using the eLBOW program (Moriarty et al., 2009). The model was refined in CNS (version 1.3) (Brünger et al., 1998) and

32

Phenix (version 1.20.1) (Adams et al., 2010). Refinement statistics are summarized in Table 3. Figures were generated with PyMOL (version 1.8) (The PyMOL Molecular Graphics System, Schrödinger, LLC) and UCSF Chimera (version 1.10) (Pettersen et al., 2004).

MD simulations under equilibrium conditions

The simulations performed under equilibrium conditions are summarized in Table 4. For simulations of pure lipid bilayers, a single cholesterol molecule was inserted in a membrane of 128 lipids at the same height, relative to the neighboring lipids, as the deep cholesterol seen in the AQP01SM:2Chol structure (Figure 5–figure supplement 1A). For simulations using a single AQP0 tetramer, the tetramer was inserted into a membrane containing ~488 lipids, either by itself (Figure 5–figure supplement 1B) or with the annular lipids observed in the AQP01SM:2Chol structure, in which case the missing atoms in the lipid acyl chains were added (Figure 5–figure supplement 1C). For simulations using a tetramer pair, only the lipids sandwiched between them in the EC structures were included and the acyl chains completed as above (Figure 5–figure supplement 1D). Here, two different arrangements of sandwiched lipids were considered: either the layer consisting of the SM lipids seen in the AQP02SM:1Chol structure or a hybrid layer replacing the two central SM lipids with the electron crystallographic (EC) deep cholesterol molecules observed in the AQP01SM:2Chol structure. In this case, both the tetramer pair and the sandwiched lipids were inserted in a membrane containing 1594 lipids.

Initial positions of the protein and annular lipids were taken from the electron crystallographic structures of AQP0 with the surrounding annular lipids obtained in N-palmitoyl sphingomyelin (SM) membranes at low (~33%) and high (~66%) cholesterol (Chol) concentrations. Initial

33

configurations of fully solvated membranes with three different cholesterol concentrations (see Table 4) were generated and equilibrated using the standard protocol of CHARMM-GUI . This equilibration process started with a Steepest Descent energy minimization step, followed by five consecutive short equilibration simulations (first three with a timestep of 1 fs, the final two with a timestep of 2 fs) with a gradual decrease in position and dihedral restraints for the lipid headgroups and a final one without position restraints. This last step was performed for at least 100 ns until the bulk membrane properties, deuterium order parameter and area per lipid, became stable and congruent with previous reports such as those by Doktorova et al. (2020) and others (Figure 5–figure supplement 2 and Figure 5–figure supplement 3). Large variations in the area per lipid occurred within the first few tens of nanoseconds, after which the area per lipid stabilized. In the particular case of the SM:CHOL = 2:1 mixture, the 64 lipid/leaflet system converged to a stable area per lipid value in the last 70 ns and the 244 lipid/leaflet system approached the same value in approximately the last 30 ns. This was a good indication that the larger system had also converged.

AQP0 with or without the EC lipids was inserted into equilibrated SM:Chol membranes using g_membed (Wolf et al., 2010; Yesylevskyy, 2007). Five simulation replicas (ten for the tetramer pair) were run for each system with a simulation time per replica of 1 µs for the tetramer pair, and 500 ns for all others. For all simulations including EC lipids, the protein was inserted and then each replica was initialized with different velocity distributions. Upon insertion, the systems with one tetramer contained from 284 to 344 lipids and the systems containing the tetramer pair from 1292 to 1318 lipids. For simulations of a single AQP0 tetramer without EC lipids, in addition to using different random starting velocities, the protein was rotated at 18º intervals such

that it faced different lipids. For simulations of a tetramer pair, the pair was rotated at 36° intervals for each replica. In the first five replicas, the tetramer pair was inserted at the center of the membrane, while in the other five replicas it was inserted at the corner of the pre-equilibrated lipid membrane. The first 100 ns of each simulation replica (the first 300 ns for the two tetramer simulations) were considered as additional equilibration time and were not included in further analysis.

All simulations were run using GROMACS (2019 version) (Abraham et al., 2015; Páll et al., 2020) using the CHARMM36 force field (Brooks et al., 2009). Periodic boundary conditions were applied. All systems were maintained at a temperature of 323 K (coupling constant of 1 ps) and a pressure of 1 bar (coupling constant of 5 ps) using the Nosé-Hoover thermostat (Hoover, 1985; Nosé, 1984) (Berendsen (Berendsen et al., 1984) in the position-restrained equilibration steps) and the Parrinello-Rahman barostat (Nosé and Klein, 1983; Parrinello and Rahman, 1981) in a semi-isotropic scheme, respectively. The chosen temperature, which was also used in a previous MD study of pure SM membranes (Niemelä et al. 2004), ensured that the lipid bilayers remained well above the liquid phase transition (Keyvanloo et al., 2018). At that Hydrogen atoms used the LINCS algorithm to solve the bond-length constraints (Hess et al., 1997), while the water molecules were constrained with the SETTLE algorithm (Miyamoto and Kollman, 1992). Simulations were run at a NaCl concentration of ~0.150 M and with the CHARMM TIP3P water model (MacKerell et al., 1998). Electrostatics were calculated using the Particle Mesh Ewald (PME) method (Darden et al., 1993; Essmann et al., 1995), splitting the direct and the reciprocal space at a distance of 0.12 nm. A Lennard Jones potential was used to treat short-range interactions in a force-switch scheme transitioning from 1.0 nm until a cut-off of 1.2 nm. The Verlet buffer scheme was utilized to consider neighboring atoms (Páll and Hess, 2013).

Force-probe MD simulations

Force-probe MD simulations on pairs of AQP0 tetramers were carried out using the same parameters used for the equilibrium simulations. Harmonic forces were applied to the center of mass of the backbone atoms of the α-helices of each tetramer, pulling them apart with a spring constant of 500 kJ/mol/nm^2 and moving the reference positions of the harmonic springs at a constant velocity at three different rates: 0.1 m/s, 0.02 m/s, and 0.004 m/s. 20 replicas were run for each rate, ranging from ~55 ns to ~900 ns. Initial configurations were taken from snapshots at 500 ns and 750 ns from each replica of the equilibrium simulations.

Methods of analysis

Cholesterol insertion depth and orientation

The membrane-insertion depth and orientation angle of all cholesterol molecules of interest were measured using gmx trajectory and gmx gangle, respectively, from the GROMACS analysis toolbox (Abraham et al., 2015; Páll et al., 2020). The simulations of cholesterol in a pure SM bilayer, of an individual AQP0 tetramer with EC lipids, and of AQP0 tetramers pairs, were all considered independently for this calculation. In the case of pure SM bilayers, only the one inserted deep cholesterol molecule was analyzed, whereas for the simulations with an individual APQ0 tetramer, we monitored separately the closest cholesterol molecule to each S1 and S2 surface center (thus, the cholesterol at the deep position was dynamically selected and the EC cholesterol molecules were free to swap positions with the surrounding bulk ones). For simulations with pairs of AQP0 tetramers, due to symmetry, the two deep cholesterol molecules sandwiched between the tetramers were considered thus doubling the sampling.

The membrane-insertion depth was defined as the position of the cholesterol oxygen atom in reference to the average z position of the phosphorus atoms of the SM molecules in the extracellular leaflet within 0.8 nm of the protein for the systems containing AQP0 tetramers, or within 3.0 nm of the monitored lipid for the systems not containing AQP0 teramers ("no-AQP0"). Accordingly, the reference (i.e., $d = 0$) was also dynamically set. The cholesterol angle was defined as the angle between the vector from the C-17 to the C-3 atom in the steroid ring and the z-axis (normal to the membrane plane).

Cholesterol distribution around AQP0 from unbiased simulations

The set of simulations with one AQP0 tetramer without the EC lipids was used to monitor the localization of cholesterol around an isolated AQP0 tetramer. The localization density was computed around every AQP0 monomer, which, due to the tetrameric structure of AQP0, effectively increased the sampling four-fold. Time-averaged density maps for the cholesterol localization were generated using GROmaρs (Briones et al., 2019). In brief, a grid of 0.1 nm in resolution, spanning the simulation box, was considered. Atomic positions were spread onto the grid by a linear combination of four Gaussian curves with amplitudes and widths taken from (Hirai et al., 2007). The density was computed separately around every monomer after least-square rigid-body fitting of their positions in the trajectories to the initial monomer position from the electron crystallography structure. The resulting four maps were then summed up using the GROmaρs mapdiff tool. Density maps were visualized with PyMOL (The PyMOL Molecular Graphics System, Schrödinger, LLC) as isosurfaces at 9σ at a maximum distance of 1 nm away from the protein. The EC lipids for each lipid composition were overlaid to their corresponding SM:Chol ratio simulation.

37

Principal Component Analysis (PCA)

PCA was carried out to analyze the relative motion of the two associated tetramers using the covar and anaeig tools from GROMACS. The covariance matrix of the positions of the backbone atoms was computed and diagonalized (Amadei et al., 1993). The equilibrium MD simulations with a pair of AQP0 tetramers containing an "SM" interface were used for these calculations. Subsequently, both sets of trajectories (for the "Chol" and "SM" interfaces) were projected on the main principal components. A least-square fitting of the C_α atoms of one of the tetramers with respect to its initial conformation, preceded the PCA calculation. Accordingly, the resulting trajectories correspond to the motion of one tetramer relative to the other (Figure 7B).

Detachment force

The force acting on the tetramers and the separation between their centers of mass was monitored over time in the force-probe MD simulations (Figure 7C–D). The noise of these curves was reduced by applying a Gaussian filter to them (order 0 and Gaussian sigma width of 100 ps). The detachment force was assumed to be the maximum registered force before the separation of the centers of mass of the two tetramers surpassed 7.3 nm (Figure 7D–E). 20 eplicas were performed for each system (Figure 7E). Box plots are presented as a function of the pulling velocity (Figure 7F). To estimate the significance and robustness of the difference in the detachment forces measured for the systems with and without deep cholesterol at the interface, we calculated the statistic and corresponding p-values, separately for each pulling velocity, using the Mann-Whitney U test (as implemented in SciPy 1.11.4 , Python 3.9.19) (Virtanen et al.,

2020), and considering the three pulling velocities at once, using the uncorrected two-way ANOVA tests (from the Statsmodel package, version 0.14.0; Seabold et al. 2010).

Molecular density maps between tetramers

The distribution of atoms at the interface between tetramers was assessed for the two paired AQP0 tetramers systems. This was achieved by computing the time-averaged density map on the surface of one tetramer that faced the adjacent tetramer. The equilibrium MD simulations of these systems were used as input for these computations. These maps were generated with GROmaρs (Briones et al., 2019) using the same calculation parameters as for the cholesterol density maps around an individual AQP0 tetramer (see above). To obtain the positional distribution of the different constituents of the system, the density was split into the contributions made by the adjacent tetramer, sphingomyelin, cholesterol, and water atoms.

Protein–protein contacts

In the simulations of pairs of AQP0 tetramers, the total number of protein–protein contacts was computed using the GROMACS gmx mindist tool, using a cutoff distance of 0.6 nm to define a contact (Figure 8–figure supplement 2). In addition, the fraction of time one residue was in contact with a residue from the opposing tetramer, T_{ij}, was quantified using ConAn (Mercadante et al., 2018) and is shown in Figure 8B. The difference in this fraction for the pairs of AQP0 tetramers without (SM) or with deep cholesterols (Chol) at the interface, $\Delta T_{ij}=T_{ij}(\text{Chol})-T_{ij}(\text{SM})$, was computed for each residue pair and is presented in Figure 8C. Finally, the average lifetime of each contact, τ_{ij}, was also obtained with ConAn and is displayed in Figure 8D.

Surface complementarity

For each of the two lipids at the center of the interface, sandwiched between AQP0 tetramers, we computed the contact area with each tetramer as $A_{Contact,i,m}=0.5(A_{Tet,m}+A_{lipid,i}-A_{Tet,m+Lipid,i})$. Here, $A_{Tet,m}$ is the surface area of tetramer m ($m = 1,2$), $A_{Lipid,i}$ is the surface area of the lipid i (either SM or Chol, $i = 1,2$) and $A_{Tet,m+Lipid,i}$ is the combined surface area of tetramer m and lipid i. We then present $A_{Contact,i}=(A_{Contact,i,1}+A_{Contact,i,2})$. This value represents the amount of the surface of lipid i that is covered by either tetramer, which, when normalized by $A_{Lipid,i}$, provides a measure of the surface complementarity between the lipids and tetramers. Consequently, a value of $A_{Contact}/A_{Lipid} = 1$ corresponds to a perfect match between the two molecular species (i.e. the entire surface area of the lipid is in contact with a tetramer), while $A_{Contact}/A_{Lipid} = 0$ indicates no match at all. In practice, neither of these two extremes is observed and rather about half of the surface of a given lipid ($A_{Contact}/A_{Lipid} = 0.5$) is in contact with one tetramer, and on fewer occasions partially with the two tetramers. $A_{Contact}/A_{Lipid}$ was computed separately for each of the two sandwiched central lipids located in the middle of the interface, either SM or Chol. Surface areas were computed using the double cubic lattice method, a variant of the Shrake-Rupley algorithm, as implemented in the gmx sasa GROMACS tool (Abraham et al., 2015; Connolly, 1983; Eisenhaber et al., 1995).

Data availability

Model coordinates with the electron diffraction data in this study were deposited in the Protein Data Bank (PDB) under accession numbers 8SJY (AQP0$_{1SM:2Chol}$) and 8SJX (AQP0$_{2SM:1Chol}$). All data are available in the wwPDB database or from authors upon request.

Acknowledgments

Additional Information

Author Contributions

P.L.C. performed biochemistry, EM data collection and processing, and structure determination. J.D.O. carried out the MD simulations. T.W. and C.A.-S. guided the project. All authors analyzed the data and prepared the manuscript.

Author ORCIDs

Po-Lin Chiu – 0000-0001-8608-7650

Juan D. Orjuela – 0000-0002-1387-3105

Bert L. de Groot – 0000-0003-3570-3534

Camilo Aponte-Santamaría – 0000-0002-8427-6965

Thomas Walz – 0000-0003-2606-2835

Declaration of Interests

The authors declare no competing interests.

References

Abraham MJ, Murtola T, Schulz R, Páll S, Smith JC, Hess B, Lindahl E. 2015. GROMACS: High performance molecular simulations through multi-level parallelism from laptops to supercomputers. *SoftwareX* **1–2**:19–25. doi:10.1016/j.softx.2015.06.001

Adams PD, Afonine PV, Bunkóczi G, Chen VB, Davis IW, Echols N, Headd JJ, Hung L-W, Kapral GJ, Grosse-Kunstleve RW, McCoy AJ, Moriarty NW, Oeffner R, Read RJ, Richardson DC, Richardson JS, Terwilliger TC, Zwart PH. 2010. PHENIX: a comprehensive Python-based system for macromolecular structure solution. *Acta Crystallogr D Biol Crystallogr* **66**:213–221. doi:10.1107/S0907444909052925

Ahmed SN, Brown DA, London E. 1997. On the origin of sphingolipid/cholesterol-rich detergent-insoluble cell membranes: physiological concentrations of cholesterol and sphingolipid induce formation of a detergent-insoluble, liquid-ordered lipid phase in model membranes. *Biochemistry* **36**:10944–10953. doi:10.1021/bi971167g

Alcalá J, Lieska N, Maisel H. 1975. Protein composition of bovine lens cortical fiber cell membranes. *Exp Eye Res* **21**:581–595. doi:10.1016/0014-4835(75)90040-8

Amadei A, Linssen AB, Berendsen HJ. 1993. Essential dynamics of proteins. *Proteins* **17**:412–425. doi:10.1002/prot.340170408

Aponte-Santamaría C, Briones R, Schenk AD, Walz T, de Groot BL. 2012. Molecular driving forces defining lipid positions around aquaporin-0. *Proc Natl Acad Sci U S A* **109**:9887–9892. doi:10.1073/pnas.1121054109

Arnarez C, Mazat J-P, Elezgaray J, Marrink S-J, Periole X. 2013. Evidence for cardiolipin binding sites on the membrane-exposed surface of the cytochrome bc1. *J Am Chem Soc* **135**:3112–3120. doi:10.1021/ja310577u

Baier CJ, Fantini J, Barrantes FJ. 2011. Disclosure of cholesterol recognition motifs in transmembrane domains of the human nicotinic acetylcholine receptor. *Sci Rep* **1**:69. doi:10.1038/srep00069

Barenholz Y. 2002. Cholesterol and other membrane active sterols: from membrane evolution to "rafts." *Prog Lipid Res* **41**:1–5. doi:10.1016/s0163-7827(01)00016-9

Belrhali H, Nollert P, Royant A, Menzel C, Rosenbusch JP, Landau EM, Pebay-Peyroula E. 1999. Protein, lipid and water organization in bacteriorhodopsin crystals: a molecular view of the purple membrane at 1.9 A resolution. *Structure* **7**:909–917. doi:10.1016/s0969-2126(99)80118-x

Berendsen HJC, Postma JPM, van Gunsteren WF, DiNola A, Haak JR. 1984. Molecular dynamics with coupling to an external bath. *J Chem Phys* **81**:3684–3690. doi:10.1063/1.448118

Bloemendal H, Zweers A, Vermorken F, Dunia I, Benedetti EL. 1972. The plasma membranes of eye lens fibres. Biochemical and structural characterization. *Cell Differ* **1**:91–106. doi:10.1016/0045-6039(72)90032-2

Briones R, Aponte-Santamaría C, de Groot BL. 2017. Localization and Ordering of Lipids Around Aquaporin-0: Protein and Lipid Mobility Effects. *Front Physiol* **8**:124. doi:10.3389/fphys.2017.00124

Briones R, Blau C, Kutzner C, de Groot BL, Aponte-Santamaría C. 2019. GROmaρs: A GROMACS-Based Toolset to Analyze Density Maps Derived from Molecular Dynamics Simulations. *Biophys J* **116**:4–11. doi:10.1016/j.bpj.2018.11.3126

Brooks BR, Brooks CL 3rd, Mackerell AD Jr, Nilsson L, Petrella RJ, Roux B, Won Y, Archontis G, Bartels C, Boresch S, Caflisch A, Caves L, Cui Q, Dinner AR, Feig M, Fischer S, Gao

J, Hodoscek M, Im W, Kuczera K, Lazaridis T, Ma J, Ovchinnikov V, Paci E, Pastor RW, Post CB, Pu JZ, Schaefer M, Tidor B, Venable RM, Woodcock HL, Wu X, Yang W, York DM, Karplus M. 2009. CHARMM: the biomolecular simulation program. *J Comput Chem* **30**:1545–1614. doi:10.1002/jcc.21287

Brown DA, London E. 2000. Structure and function of sphingolipid- and cholesterol-rich membrane rafts. *J Biol Chem* **275**:17221–17224. doi:10.1074/jbc.R000005200

Brünger AT, Adams PD, Clore GM, DeLano WL, Gros P, Grosse-Kunstleve RW, Jiang JS, Kuszewski J, Nilges M, Pannu NS, Read RJ, Rice LM, Simonson T, Warren GL. 1998. Crystallography & NMR system: A new software suite for macromolecular structure determination. *Acta Crystallogr D Biol Crystallogr* **54**:905–921. doi:10.1107/s0907444998003254

Burley SK, Petsko GA. 1985. Aromatic-aromatic interaction: a mechanism of protein structure stabilization. *Science* **229**:23–28. doi:10.1126/science.3892686

Buzhynskyy N, Hite RK, Walz T, Scheuring S. 2007. The supramolecular architecture of junctional microdomains in native lens membranes. *EMBO Rep* **8**:51–55. doi:10.1038/sj.embor.7400858

Chiu P-L, Li X, Li Z, Beckett B, Brilot AF, Grigorieff N, Agard DA, Cheng Y, Walz T. 2015. Evaluation of super-resolution performance of the K2 electron-counting camera using 2D crystals of aquaporin-0. *J Struct Biol* **192**:163–173. doi:10.1016/j.jsb.2015.08.015

Connolly ML. 1983. Analytical molecular surface calculation. *J Appl Crystallogr* **16**:548–558. doi:10.1107/S0021889883010985

Corradi V, Mendez-Villuendas E, Ingólfsson HI, Gu R-X, Siuda I, Melo MN, Moussatova A, DeGagné LJ, Sejdiu BI, Singh G, Wassenaar TA, Delgado Magnero K, Marrink SJ,

Tieleman DP. 2018. Lipid-Protein Interactions Are Unique Fingerprints for Membrane Proteins. *ACS Cent Sci* **4**:709–717. doi:10.1021/acscentsci.8b00143

Corradi V, Sejdiu BI, Mesa-Galloso H, Abdizadeh H, Noskov SY, Marrink SJ, Tieleman DP. 2019. Emerging Diversity in Lipid-Protein Interactions. *Chem Rev* **119**:5775–5848. doi:10.1021/acs.chemrev.8b00451

Crnjar A, Molteni C. 2021. Cholesterol content in the membrane promotes key lipid-protein interactions in a pentameric serotonin-gated ion channel. *Biointerphases* **15**:061018. doi:10.1116/6.0000561

Darden T, York D, Pedersen L. 1993. Particle mesh Ewald: AnN·log(N) method for Ewald sums in large systems. *J Chem Phys* **98**:10089–10092. doi:10.1063/1.464397

de Meyer F, Smit B. 2009. Effect of cholesterol on the structure of a phospholipid bilayer. *Proc Natl Acad Sci U S A* **106**:3654–3658. doi:10.1073/pnas.0809959106

de Meyer FJ-M, Benjamini A, Rodgers JM, Misteli Y, Smit B. 2010. Molecular simulation of the DMPC-cholesterol phase diagram. *J Phys Chem B* **114**:10451–10461. doi:10.1021/jp103903s

Devaux PF. 1991. Static and dynamic lipid asymmetry in cell membranes. *Biochemistry* **30**:1163–1173. doi:10.1021/bi00219a001

Doktorova M, Kučerka N, Kinnun JJ, Pan J, Marquardt D, Scott HL, Venable RM, Pastor RW, Wassall SR, Katsaras J, Heberle FA. 2020. Molecular Structure of Sphingomyelin in Fluid Phase Bilayers Determined by the Joint Analysis of Small-Angle Neutron and X-ray Scattering Data. *J Phys Chem B* **124**:5186–5200. doi:10.1021/acs.jpcb.0c03389

Eisenhaber F, Lijnzaad P, Argos P, Sander C, Scharf M. 1995. The double cubic lattice method: Efficient approaches to numerical integration of surface area and volume and to dot

46

surface contouring of molecular assemblies. *J Comput Chem* **16**:273–284. doi:10.1002/jcc.540160303

Elkins MR, Sergeyev IV, Hong M. 2018. Determining Cholesterol Binding to Membrane Proteins by Cholesterol 13C Labeling in Yeast and Dynamic Nuclear Polarization NMR. *J Am Chem Soc* **140**:15437–15449. doi:10.1021/jacs.8b09658

Elkins MR, Williams JK, Gelenter MD, Dai P, Kwon B, Sergeyev IV, Pentelute BL, Hong M. 2017. Cholesterol-binding site of the influenza M2 protein in lipid bilayers from solid-state NMR. *Proc Natl Acad Sci U S A* **114**:12946–12951. doi:10.1073/pnas.1715127114

Emsley P, Cowtan K. 2004. Coot: model-building tools for molecular graphics. *Acta Crystallogr D Biol Crystallogr* **60**:2126–2132. doi:10.1107/S0907444904019158

Engelman DM. 2005. Membranes are more mosaic than fluid. *Nature* **438**:578–580. doi:10.1038/nature04394

Epand RM, Epand RF. 2004. Non-raft forming sphingomyelin-cholesterol mixtures. *Chem Phys Lipids* **132**:37–46. doi:10.1016/j.chemphyslip.2004.09.012

Essmann U, Perera L, Berkowitz ML, Darden T, Lee H, Pedersen LG. 1995. A smooth particle mesh Ewald method. *J Chem Phys* **103**:8577–8593. doi:10.1063/1.470117

Fantini J, Barrantes FJ. 2013. How cholesterol interacts with membrane proteins: an exploration of cholesterol-binding sites including CRAC, CARC, and tilted domains. *Front Physiol* **4**:31. doi:10.3389/fphys.2013.00031

Fantini J, Carlus D, Yahi N. 2011. The fusogenic tilted peptide (67-78) of α-synuclein is a cholesterol binding domain. *Biochim Biophys Acta* **1808**:2343–2351. doi:10.1016/j.bbamem.2011.06.017

Fleschner CR, Cenedella RJ. 1991. Lipid composition of lens plasma membrane fractions enriched in fiber junctions. *J Lipid Res* **32**:45–53.

Gahbauer S, Böckmann RA. 2016. Membrane-Mediated Oligomerization of G Protein Coupled Receptors and Its Implications for GPCR Function. *Front Physiol* **7**:494. doi:10.3389/fphys.2016.00494

Genheden S, Essex JW, Lee AG. 2017. G protein coupled receptor interactions with cholesterol deep in the membrane. *Biochim Biophys Acta Biomembr* **1859**:268–281. doi:10.1016/j.bbamem.2016.12.001

Ghysels A, Krämer A, Venable RM, Teague WE Jr, Lyman E, Gawrisch K, Pastor RW. 2019. Permeability of membranes in the liquid ordered and liquid disordered phases. *Nat Commun* **10**:5616. doi:10.1038/s41467-019-13432-7

Gimpl G. 2016. Interaction of G protein coupled receptors and cholesterol. *Chem Phys Lipids* **199**:61–73. doi:10.1016/j.chemphyslip.2016.04.006

Gipson B, Zeng X, Stahlberg H. 2007a. 2dx_merge: data management and merging for 2D crystal images. *J Struct Biol* **160**:375–384. doi:10.1016/j.jsb.2007.09.011

Gipson B, Zeng X, Zhang ZY, Stahlberg H. 2007b. 2dx--user-friendly image processing for 2D crystals. *J Struct Biol* **157**:64–72. doi:10.1016/j.jsb.2006.07.020

Gonen T, Cheng Y, Sliz P, Hiroaki Y, Fujiyoshi Y, Harrison SC, Walz T. 2005. Lipid-protein interactions in double-layered two-dimensional AQP0 crystals. *Nature* **438**:633–638. doi:10.1038/nature04321

Gonen T, Sliz P, Kistler J, Cheng Y, Walz T. 2004. Aquaporin-0 membrane junctions reveal the structure of a closed water pore. *Nature* **429**:193–197. doi:10.1038/nature02503

Gorin MB, Yancey SB, Cline J, Revel JP, Horwitz J. 1984. The major intrinsic protein (MIP) of the bovine lens fiber membrane: characterization and structure based on cDNA cloning. *Cell* **39**:49–59. doi:10.1016/0092-8674(84)90190-9

Gu R-X, Baoukina S, Tieleman DP. 2019. Cholesterol Flip-Flop in Heterogeneous Membranes. *J Chem Theory Comput* **15**:2064–2070. doi:10.1021/acs.jctc.8b00933

Gupta K, Donlan JAC, Hopper JTS, Uzdavinys P, Landreh M, Struwe WB, Drew D, Baldwin AJ, Stansfeld PJ, Robinson CV. 2017. The role of interfacial lipids in stabilizing membrane protein oligomers. *Nature* **541**:421–424. doi:10.1038/nature20820

Gyobu N, Tani K, Hiroaki Y, Kamegawa A, Mitsuoka K, Fujiyoshi Y. 2004. Improved specimen preparation for cryo-electron microscopy using a symmetric carbon sandwich technique. *J Struct Biol* **146**:325–333. doi:10.1016/j.jsb.2004.01.012

Hanson MA, Cherezov V, Griffith MT, Roth CB, Jaakola V-P, Chien EYT, Velasquez J, Kuhn P, Stevens RC. 2008. A specific cholesterol binding site is established by the 2.8 A structure of the human beta2-adrenergic receptor. *Structure* **16**:897–905. doi:10.1016/j.str.2008.05.001

Hanulová M, Weiss M. 2012. Protein sorting and membrane-mediated interactions. *Biophys Rev* **4**:117–124. doi:10.1007/s12551-012-0069-8

Hess B, Bekker H, Berendsen HJC, Fraaije JGEM. 1997. LINCS: A linear constraint solver for molecular simulations. *J Comput Chem* **18**:1463–1472. doi:10.1002/(sici)1096-987x(199709)18:12<1463::aid-jcc4>3.0.co;2-h

Hirai T, Mitsuoka K, Kidera A, Fujiyoshi Y. 2007. Simulation of charge effects on density maps obtained by high-resolution electron crystallography. *J Electron Microsc (Tokyo)* **56**:131–140. doi:10.1093/jmicro/dfm019

Hite RK, Chiu P-L, Schuller JM, Walz T. 2015. Effect of lipid head groups on double-layered two-dimensional crystals formed by aquaporin-0. *PLoS One* **10**:e0117371. doi:10.1371/journal.pone.0117371

Hite RK, Li Z, Walz T. 2010. Principles of membrane protein interactions with annular lipids deduced from aquaporin-0 2D crystals. *EMBO J* **29**:1652–1658. doi:10.1038/emboj.2010.68

Hoover WG. 1985. Canonical dynamics: Equilibrium phase-space distributions. *Phys Rev A Gen Phys* **31**:1695–1697. doi:10.1103/physreva.31.1695

Huang C-S, Yu X, Fordstrom P, Choi K, Chung BC, Roh S-H, Chiu W, Zhou M, Min X, Wang Z. 2020. Cryo-EM structures of NPC1L1 reveal mechanisms of cholesterol transport and ezetimibe inhibition. *Sci Adv* **6**:eabb1989. doi:10.1126/sciadv.abb1989

Jo S, Kim T, Iyer VG, Im W. 2008. CHARMM-GUI: a web-based graphical user interface for CHARMM. *J Comput Chem* **29**:1859–1865. doi:10.1002/jcc.20945

Jo S, Rui H, Lim JB, Klauda JB, Im W. 2010. Cholesterol flip-flop: insights from free energy simulation studies. *J Phys Chem B* **114**:13342–13348. doi:10.1021/jp108166k

Karnovsky MJ, Kleinfeld AM, Hoover RL, Klausner RD. 1982. The concept of lipid domains in membranes. *J Cell Biol* **94**:1–6. doi:10.1083/jcb.94.1.1

Keyvanloo A, Shaghaghi M, Zuckermann MJ, Thewalt JL. 2018. The phase behavior and organization of sphingomyelin/cholesterol membranes: a deuterium NMR study. Biophys J 114:1344–1356. doi: 10.1016/j.bpj.2018.01.024

Khunweeraphong N, Mitchell-White J, Szöllősi D, Hussein T, Kuchler K, Kerr ID, Stockner T, Lee J-Y. 2020. Picky ABCG5/G8 and promiscuous ABCG2 - a tale of fatty diets and drug toxicity. *FEBS Lett* **594**:4035–4058. doi:10.1002/1873-3468.13938

Kistler J, Bullivant S. 1980. Lens gap junctions and orthogonal arrays are unrelated. *FEBS Lett* **111**:73–78. doi:10.1016/0014-5793(80)80764-2

Korade Z, Kenworthy AK. 2008. Lipid rafts, cholesterol, and the brain. *Neuropharmacology* **55**:1265–1273. doi:10.1016/j.neuropharm.2008.02.019

Kumar VV. 1991. Complementary molecular shapes and additivity of the packing parameter of lipids. *Proc Natl Acad Sci U S A* **88**:444–448. doi:10.1073/pnas.88.2.444

Kurth M, Lolicato F, Sandoval-Perez A, Amaya-Espinosa H, Teslenko A, Sinning I, Beck R, Brügger B, Aponte-Santamaría C. 2020. Cholesterol Localization around the Metabotropic Glutamate Receptor 2. *J Phys Chem B* **124**:9061–9078. doi:10.1021/acs.jpcb.0c05264

Lafleur M, Bloom M, Cullis PR. 1990. Lipid polymorphism and hydrocarbon order. *Biochem Cell Biol* **68**:1–8. doi:10.1139/o90-001

Laganowsky A, Reading E, Allison TM, Ulmschneider MB, Degiacomi MT, Baldwin AJ, Robinson CV. 2014. Membrane proteins bind lipids selectively to modulate their structure and function. *Nature* **510**:172–175. doi:10.1038/nature13419

Lee AG. 2018. A Database of Predicted Binding Sites for Cholesterol on Membrane Proteins, Deep in the Membrane. *Biophys J* **115**:522–532. doi:10.1016/j.bpj.2018.06.022

Lee J, Cheng X, Jo S, MacKerell AD Jr, Klauda JB, Im W. 2016. CHARMM-GUI Input Generator for NAMD, Gromacs, Amber, Openmm, and CHARMM/OpenMM Simulations using the CHARMM36 Additive Force Field. *Biophys J* **110**:641a. doi:10.1016/j.bpj.2015.11.3431

Li H, Papadopoulos V. 1998. Peripheral-type benzodiazepine receptor function in cholesterol transport. Identification of a putative cholesterol recognition/interaction amino acid

sequence and consensus pattern. *Endocrinology* **139**:4991–4997. doi:10.1210/endo.139.12.6390

Li X, Mooney P, Zheng S, Booth CR, Braunfeld MB, Gubbens S, Agard DA, Cheng Y. 2013. Electron counting and beam-induced motion correction enable near-atomic-resolution single-particle cryo-EM. *Nat Methods* **10**:584–590. doi:10.1038/nmeth.2472

Lingwood D, Simons K. 2010. Lipid rafts as a membrane-organizing principle. *Science* **327**:46–50. doi:10.1126/science.1174621

Liscum L, Munn NJ. 1999. Intracellular cholesterol transport. *Biochim Biophys Acta* **1438**:19–37. doi:10.1016/s1388-1981(99)00043-8

MacKerell AD, Bashford D, Bellott M, Dunbrack RL, Evanseck JD, Field MJ, Fischer S, Gao J, Guo H, Ha S, Joseph-McCarthy D, Kuchnir L, Kuczera K, Lau FT, Mattos C, Michnick S, Ngo T, Nguyen DT, Prodhom B, Reiher WE, Roux B, Schlenkrich M, Smith JC, Stote R, Straub J, Watanabe M, Wiórkiewicz-Kuczera J, Yin D, Karplus M. 1998. All-atom empirical potential for molecular modeling and dynamics studies of proteins. *J Phys Chem B* **102**:3586–3616. doi:10.1021/jp973084f

Marino KA, Prada-Gracia D, Provasi D, Filizola M. 2016. Impact of Lipid Composition and Receptor Conformation on the Spatio-temporal Organization of μ-Opioid Receptors in a Multi-component Plasma Membrane Model. *PLoS Comput Biol* **12**:e1005240. doi:10.1371/journal.pcbi.1005240

Marsh D. 2010. Liquid-ordered phases induced by cholesterol: a compendium of binary phase diagrams. *Biochim Biophys Acta* **1798**:688–699. doi:10.1016/j.bbamem.2009.12.027

Mathiharan YK, Glaaser IW, Zhao Y, Robertson MJ, Skiniotis G, Slesinger PA. 2021. Structural insights into GIRK2 channel modulation by cholesterol and PIP2. *Cell Rep* **36**:109619. doi:10.1016/j.celrep.2021.109619

McCoy AJ, Grosse-Kunstleve RW, Adams PD, Winn MD, Storoni LC, Read RJ. 2007. Phaser crystallographic software. *J Appl Crystallogr* **40**:658–674. doi:10.1107/S0021889807021206

McGaughey GB, Gagné M, Rappé AK. 1998. pi-Stacking interactions. Alive and well in proteins. *J Biol Chem* **273**:15458–15463. doi:10.1074/jbc.273.25.15458

Mercadante D, Gräter F, Daday C. 2018. CONAN: A Tool to Decode Dynamical Information from Molecular Interaction Maps. *Biophys J* **114**:1267–1273. doi:10.1016/j.bpj.2018.01.033

Miyamoto S, Kollman PA. 1992. Settle: An analytical version of the SHAKE and RATTLE algorithm for rigid water models. *J Comput Chem* **13**:952–962. doi:10.1002/jcc.540130805

Moriarty NW, Grosse-Kunstleve RW, Adams PD. 2009. electronic Ligand Builder and Optimization Workbench (eLBOW): a tool for ligand coordinate and restraint generation. *Acta Crystallogr D Biol Crystallogr* **65**:1074–1080. doi:10.1107/S0907444909029436

Nicolson GL. 2014. The Fluid-Mosaic Model of Membrane Structure: still relevant to understanding the structure, function and dynamics of biological membranes after more than 40 years. *Biochim Biophys Acta* **1838**:1451–1466. doi:10.1016/j.bbamem.2013.10.019

Niemelä P, Hyvönen MT, Vattulainen I. 2004. Structure and dynamics of sphingomyelin bilayer: insight gained through systematic comparison to phosphatidylcholine. Biophys J 87:2976–2989. doi: 10.1529/biophysj.104.048702

Niemelä PS, Miettinen MS, Monticelli L, Hammaren H, Bjelkmar P, Murtola T, Lindahl E, Vattulainen I. 2010. Membrane proteins diffuse as dynamic complexes with lipids. *J Am Chem Soc* **132**:7574–7575. doi:10.1021/ja101481b

Nishio M, Umezawa Y, Hirota M, Takeuchi Y. 1995. The CH/π interaction: Significance in molecular recognition. *Tetrahedron* **51**:8665–8701. doi:10.1016/0040-4020(94)01066-9

Niu S-L, Litman BJ. 2002. Determination of membrane cholesterol partition coefficient using a lipid vesicle-cyclodextrin binary system: effect of phospholipid acyl chain unsaturation and headgroup composition. *Biophys J* **83**:3408–3415. doi:10.1016/S0006-3495(02)75340-X

Nosé S. 1984. A molecular dynamics method for simulations in the canonical ensemble. *Mol Phys* **52**:255–268. doi:10.1080/00268978400101201

Nosé S, Klein ML. 1983. Constant pressure molecular dynamics for molecular systems. *Mol Phys* **50**:1055–1076. doi:10.1080/00268978300102851

O'Connor JW, Klauda JB. 2011. Lipid membranes with a majority of cholesterol: applications to the ocular lens and aquaporin 0. *J Phys Chem B* **115**:6455–6464. doi:10.1021/jp108650u

Páll S, Hess B. 2013. A flexible algorithm for calculating pair interactions on SIMD architectures. *Comput Phys Commun* **184**:2641–2650. doi:10.1016/j.cpc.2013.06.003

Páll S, Zhmurov A, Bauer P, Abraham M, Lundborg M, Gray A, Hess B, Lindahl E. 2020. Heterogeneous parallelization and acceleration of molecular dynamics simulations in GROMACS. *J Chem Phys* **153**:134110. doi:10.1063/5.0018516

Pandit SA, Khelashvili G, Jakobsson E, Grama A, Scott HL. 2007. Lateral organization in lipid-cholesterol mixed bilayers. *Biophys J* **92**:440–447. doi:10.1529/biophysj.106.093864

Parrinello M, Rahman A. 1981. Polymorphic transitions in single crystals: A new molecular dynamics method. *J Appl Phys* **52**:7182–7190. doi:10.1063/1.328693

Pettersen EF, Goddard TD, Huang CC, Couch GS, Greenblatt DM, Meng EC, Ferrin TE. 2004. UCSF Chimera--a visualization system for exploratory research and analysis. *J Comput Chem* **25**:1605–1612. doi:10.1002/jcc.20084

Quinn PJ, Wolf C. 2009. The liquid-ordered phase in membranes. *Biochim Biophys Acta* **1788**:33–46. doi:10.1016/j.bbamem.2008.08.005

Raguz M, Mainali L, Widomska J, Subczynski WK. 2011. The immiscible cholesterol bilayer domain exists as an integral part of phospholipid bilayer membranes. *Biochim Biophys Acta* **1808**:1072–1080. doi:10.1016/j.bbamem.2010.12.019

Róg T, Pasenkiewicz-Gierula M. 2006. Cholesterol-sphingomyelin interactions: a molecular dynamics simulation study. *Biophys J* **91**:3756–3767. doi:10.1529/biophysj.106.080887

Sarkar P, Chattopadhyay A. 2020. Cholesterol interaction motifs in G protein-coupled receptors: Slippery hot spots? *Wiley Interdiscip Rev Syst Biol Med* **12**:e1481. doi:10.1002/wsbm.1481

Schenk AD, Philippsen A, Engel A, Walz T. 2013. A pipeline for comprehensive and automated processing of electron diffraction data in IPLT. *J Struct Biol* **182**:173–185. doi:10.1016/j.jsb.2013.02.017

Schmidt U, Guigas G, Weiss M. 2008. Cluster formation of transmembrane proteins due to hydrophobic mismatching. *Phys Rev Lett* **101**:128104. doi:10.1103/PhysRevLett.101.128104

Schroeder F, Jefferson JR, Kier AB, Knittel J, Scallen TJ, Wood WG, Hapala I. 1991. Membrane cholesterol dynamics: cholesterol domains and kinetic pools. *Proc Soc Exp Biol Med* **196**:235–252. doi:10.3181/00379727-196-43185

Seabold S, Perktold J. 2010. Statsmodels: econometric and statistical modeling with python. SciPy 7:1

Seelig J. 1977. Deuterium magnetic resonance: theory and application to lipid membranes. *Q Rev Biophys* **10**:353–418. doi:10.1017/s0033583500002948

Shinoda T, Ogawa H, Cornelius F, Toyoshima C. 2009. Crystal structure of the sodium-potassium pump at 2.4 A resolution. *Nature* **459**:446–450. doi:10.1038/nature07939

Silvius JR. 2003. Role of cholesterol in lipid raft formation: lessons from lipid model systems. *Biochim Biophys Acta* **1610**:174–183. doi:10.1016/s0005-2736(03)00016-6

Simons K, Ikonen E. 1997. Functional rafts in cell membranes. *Nature* **387**:569–572. doi:10.1038/42408

Simons K, Toomre D. 2000. Lipid rafts and signal transduction. *Nat Rev Mol Cell Biol* **1**:31–39. doi:10.1038/35036052

Stansfeld PJ, Jefferys EE, Sansom MSP. 2013. Multiscale simulations reveal conserved patterns of lipid interactions with aquaporins. *Structure* **21**:810–819. doi:10.1016/j.str.2013.03.005

Stier A, Sackmann E. 1973. Spin labels as enzyme substrates. Heterogeneous lipid distribution in liver microsomal membranes. *Biochim Biophys Acta* **311**:400–408. doi:10.1016/0005-2736(73)90320-9

Taghon GJ, Rowe JB, Kapolka NJ, Isom DG. 2021. Predictable cholesterol binding sites in GPCRs lack consensus motifs. *Structure* **29**:499-506.e3. doi:10.1016/j.str.2021.01.004

Valpuesta JM, Carrascosa JL, Henderson R. 1994. Analysis of electron microscope images and electron diffraction patterns of thin crystals of phi 29 connectors in ice. *J Mol Biol* **240**:281–287. doi:10.1006/jmbi.1994.1445

van Meer G, Voelker DR, Feigenson GW. 2008. Membrane lipids: where they are and how they behave. *Nat Rev Mol Cell Biol* **9**:112–124. doi:10.1038/nrm2330

Vereb G, Szöllosi J, Matkó J, Nagy P, Farkas T, Vigh L, Mátyus L, Waldmann TA, Damjanovich S. 2003. Dynamic, yet structured: The cell membrane three decades after the Singer-Nicolson model. *Proc Natl Acad Sci U S A* **100**:8053–8058. doi:10.1073/pnas.1332550100

Virtanen P, Gommers R, Oliphant TE, Haberland M, Reddy T, Cournapeau D, Burovski E, Peterson P, Weckesser W, Bright J, van der Walt SJ, Brett M, Wilson J, Millman KJ, Mayorov N, Nelson ARJ, Jones E, Kern R, Larson E, Carey CJ, Polat İ, Feng Y, Moore EW, VanderPlas J, Laxalde D, Perktold J, Cimrman R, Henriksen I, Quintero EA, Harris CR, Archibald AM, Ribeiro AH, Pedregosa F, van Mulbregt P, SciPy 1.0 Contributors. 2020. SciPy 1.0: fundamental algorithms for scientific computing in Python. *Nat Methods* **17**:261–272. doi:10.1038/s41592-019-0686-2

Wang Y, Lyons JA, Timcenko M, Kümmerer F, de Groot BL, Nissen P, Gapsys V, Lindorff-Larsen K. 2024. Substrate transport and specificity in a phospholipid flippase. bioRxiv 2020.06.24.169771. doi: https://doi.org/10.1101/2020.06.24.169771

Webby MN, Oluwole AO, Pedebos C, Inns PG, Olerinyova A, Prakaash D, Housden NG, Benn G, Sun D, Hoogenboom BW, Kukura P, Mohammed S, Robinson CV, Khalid S, Kleanthous C. 2022. Lipids mediate supramolecular outer membrane protein assembly in bacteria. *Sci Adv* **8**:eadc9566. doi:10.1126/sciadv.adc9566

Winn MD, Ballard CC, Cowtan KD, Dodson EJ, Emsley P, Evans PR, Keegan RM, Krissinel EB, Leslie AGW, McCoy A, McNicholas SJ, Murshudov GN, Pannu NS, Potterton EA, Powell HR, Read RJ, Vagin A, Wilson KS. 2011. Overview of the CCP4 suite and current developments. *Acta Crystallogr D Biol Crystallogr* **67**:235–242. doi:10.1107/S0907444910045749

Wolf MG, Hoefling M, Aponte-Santamaría C, Grubmüller H, Groenhof G. 2010. g_membed: Efficient insertion of a membrane protein into an equilibrated lipid bilayer with minimal perturbation. *J Comput Chem* **31**:2169–2174. doi:10.1002/jcc.21507

Wu H, Wang C, Gregory KJ, Han GW, Cho HP, Xia Y, Niswender CM, Katritch V, Meiler J, Cherezov V, Conn PJ, Stevens RC. 2014. Structure of a class C GPCR metabotropic glutamate receptor 1 bound to an allosteric modulator. *Science* **344**:58–64. doi:10.1126/science.1249489

Yesylevskyy SO. 2007. ProtSqueeze: simple and effective automated tool for setting up membrane protein simulations. *J Chem Inf Model* **47**:1986–1994. doi:10.1021/ci600553y

Zampighi G, Simon SA, Robertson JD, McIntosh TJ, Costello MJ. 1982. On the structural organization of isolated bovine lens fiber junctions. *J Cell Biol* **93**:175–189. doi:10.1083/jcb.93.1.175

Zelenka PS. 1984. Lens lipids. *Curr Eye Res* **3**:1337–1359. doi:10.3109/02713688409007421

Zhang M, Mileykovskaya E, Dowhan W. 2002. Gluing the respiratory chain together. Cardiolipin is required for supercomplex formation in the inner mitochondrial membrane. *J Biol Chem* **277**:43553–43556. doi:10.1074/jbc.C200551200

Zheng L, McQuaw CM, Ewing AG, Winograd N. 2007. Sphingomyelin/phosphatidylcholine and cholesterol interactions studied by imaging mass spectrometry. *J Am Chem Soc* **129**:15730–15731. doi:10.1021/ja0741675

Table 1. Internal phase residuals of all rectangular plane groups for an image of an AQP0 crystal in a pure cholesterol membrane.

Spacegroup	Phase residual (degrees)[a]	Number of comparisons	Target residual (degrees)[b]
$p1$	12.5[c]	240	
$p2$	33.8	120	17.8
$p12b$	14.5[d]	108	12.9
$p12a$	31.7	109	12.9
$p12_1b$	83.7	108	12.9
$p12_1a$	80.0	109	12.9
$c12b$	14.5[d]	108	12.9
$c12a$	31.7	109	12.9
$p222$	27.0	337	14.4
$p222_1b$	60.0	337	14.4
$p222_1a$	68.2	337	14.4
$p22_12_1$	69.7	337	14.4
$c222$	27.0	337	14.4
$p4$	26.3	352	14.3
$p422$	**24.5**	**791**	**13.3**
$p42_12$	62.6	791	13.3

Internal residuals were determined using the ALLSPACE program (Valpuesta et al., 1994) using spots from IQ1 to IQ5 to a resolution of 6 Å.

a. Phase residual *versus* other spots (90° random).

b. Target residual based on the statistics taking Friedel weight into account.

c. Note that no phase comparison is possible in space group $p1$, so that the listed numbers are theoretical phase residuals based on the signal-to-noise ratio of the observed diffraction spots in the Fourier transform.

d. Within 5° of target residual.

Table 2. Phase residuals for the merging of 15 images of AQP0 2D crystals in pure cholesterol membranes.

Plane group symmetry	$p422$
Unit cell dimensions	$a = 65.5$ Å, $b = 65.5$ Å, and $\gamma = 90°$
Number of processed electron micrographs	15
Resolution limit for merging	3.0 Å
Number of phases	2,773
Phase residuals in resolution bins	
1000.0 Å – 11.6 Å	21.7°
11.6 Å – 8.2 Å	31.2°
8.2 Å – 6.7 Å	34.1°
6.7 Å – 5.8 Å	47.2°
5.8 Å – 5.2 Å	43.7°
5.2 Å – 4.7 Å	50.4°
4.7 Å – 4.4 Å	58.0°
4.4 Å – 4.1 Å	62.3°
4.1 Å – 3.9 Å	62.3°
3.9 Å – 3.7 Å	64.0°
3.7 Å – 3.5 Å	70.8°
3.5 Å – 3.4 Å	69.1°
3.4 Å – 3.2 Å	71.0°
3.2 Å – 3.1 Å	88.0°
3.1 Å – 3.0 Å	86.0°
Overall	54.5°

Table 3. Statistics of electron crystallographic structures for AQP0 in sphingomyelin/ cholesterol membranes.

	2SM:1Chol	1SM:2Chol
Crystal parameters		
Space group	*p*422	
Unit cell constants	$a = b = 65.5$ Å, $\gamma = 90°$	
Assumed thickness	200 Å	
Electron diffraction		
Diffraction patterns	214	241
	(0°:16; 20°:19; 45°:77; 60°:84; 65°:17; 70°:1)	(0°:15; 20°:18; 45°:51; 60°:86; 65°:30; 70°:41)
Maximum tilt angle	71.72°	72.35°
Upper resolution limit for merging	2.3 Å	2.3 Å
$R_{Friedel}$	0.149	0.138
R_{merge}	0.216	0.199
Observed amplitudes	122,501	127,703
Unique reflections	16,437	17031
Minimum of $F_{obs}/Sigma_{obs}$	1.33	1.33
Fourier space sampled	87.0%	90.7%
Multiplicity	6.2	6.3
	(2.3 Å: 4.9)	(2.3 Å: 4.6)
Crystallographic refinement		
Resolution range	13.8 – 2.35 Å	11.8 – 2.35 Å
R_{work}/R_{free} [a]	0.260 / 0.286	0.262 / 0.287
Atoms		
Protein	1,663	1,663
Lipids	336	341
Water	11	11
RMS deviation		
Bond length (Å)	0.008	0.005
Bond angle (degrees)	1.096	0.842
Model validation		
Clashscore	8.86	6.98
MolProbity	1.79	1.79

Rotamer outliers (%)	0.00	0.60
C-beta deviation	0	0
Ramachandran plot (%)		
Disallowed	0.00	0.00
Allowed	4.59	5.96
Favored	95.41	94.04

a. R_{free} was calculated from randomly selected 10% of total reflections, and R_{work} was calculated from the remaining 90% of reflections.

Table 4. Summary of the simulations.

Scheme	Protein system	Membrane system	Pulling rate (m/s)	Number of replicas	Length per replica (ns)
Equilibrium simulations	No AQP0	Pure SM	N/A	5	500
		2:1 SM:Chol			
		1:2 SM:Chol			
	One AQP0 tetramer without EC lipids	Pure SM		5	500
		2:1 SM:Chol			
		1:2 SM:Chol			
	One AQP0 tetramer with EC lipids	2:1 SM:Chol		5	500
		1:2 SM:Chol			
	Two AQP0 tetramers with deep cholesterol	Pure SM		10	1000
	Two AQP0 tetramer without deep cholesterol	Pure SM			
Force probe	Two AQP0 tetramers with deep cholesterol	Pure SM	0.1	20 replicas for each velocity	~55
			0.02		~230
			0.004		~900
	Two AQP0 tetramers without deep cholesterol	Pure SM	0.1	20 replicas for each velocity	~55
			0.02		~230
			0.004		~900
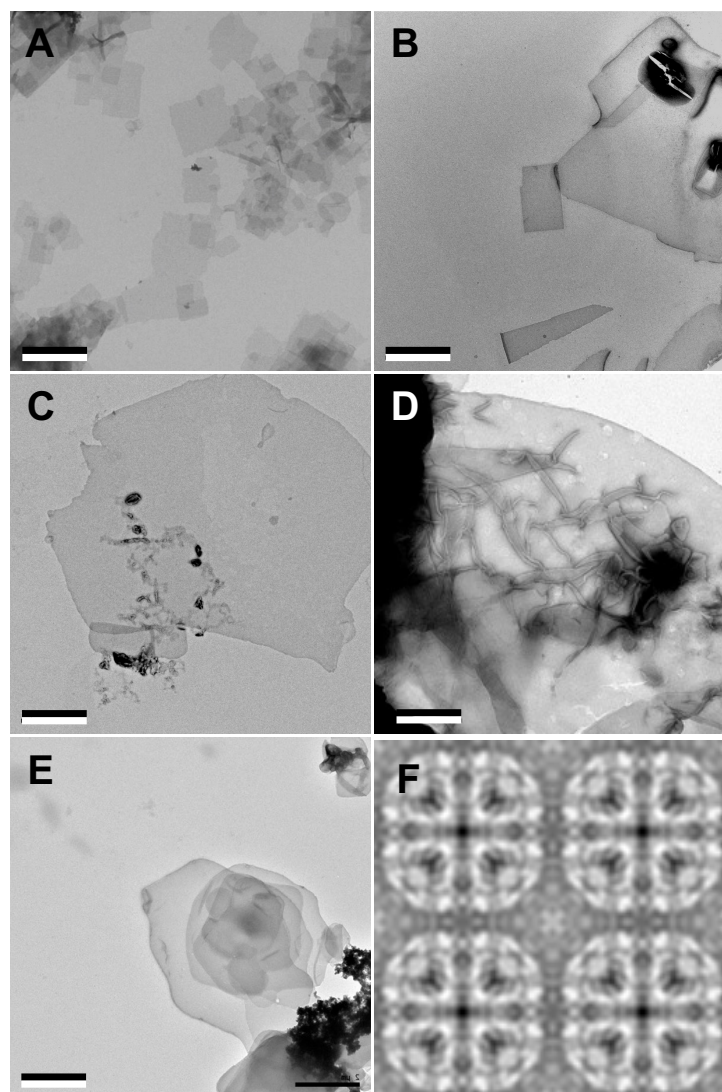
Figure 1. AQP0 forms 2D crystals with all tested sphingomyelin/cholesterol mixtures. (**A-E**) AQP0 purified from sheep lenses was reconstituted with pure sphingomyelin (A), sphingomyelin/cholesterol mixtures at molar ratios of 2:1 (B), 1:2 (C), and 1:4 (D), as well a pure cholesterol (E). AQP0 was reconstituted under all conditions and formed diffracting 2D crystals. The scale bars are 2 μm. (**F**) Projection map of AQP0 reconstituted with pure cholesterol at 3.2 Å resolution. The 2D crystals show $p422$ symmetry and have the typical lattice constants for AQP0 crystals of $a = b = 65.5$ Å, and $\gamma = 90°$. The panel shows two-by-two unit cells. See also Figure 1–figure supplements 1 and 2 and Tables 1 and 2.
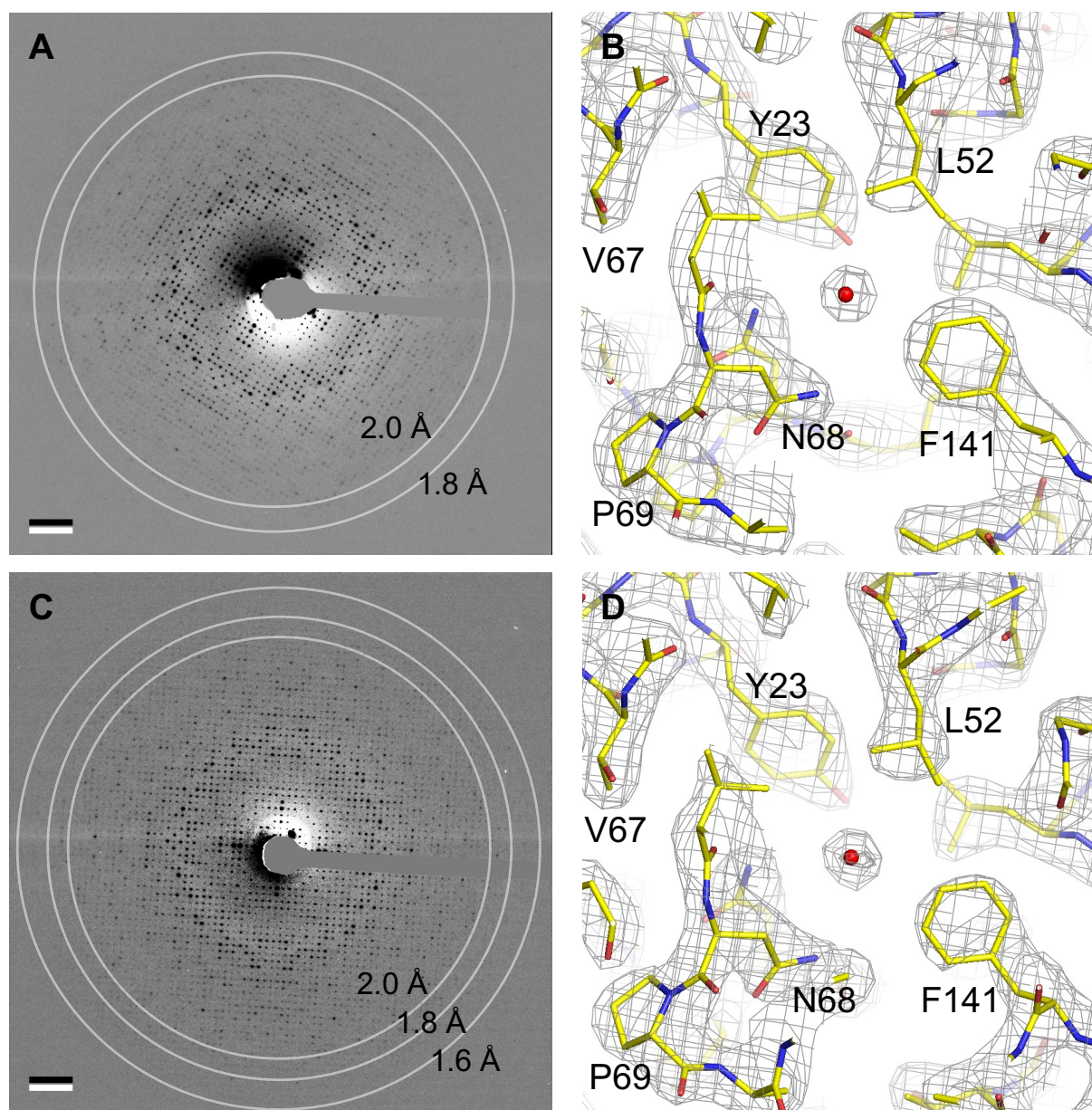
Figure 2. Electron crystallography provides structures of AQP0 in sphingomyelin/ cholesterol bilayers at 2.5-Å resolution. (**A**) Electron diffraction pattern of an untilted AQP0 2D crystal reconstituted at a sphingomyelin:cholesterol ratio of 2:1, showing reflections to ~2 Å resolution. Scale bar indicates $(10 \text{ Å})^{-1}$. (**B**) Density map at 2.5 Å resolution used to build the $AQP0_{2SM:1Chol}$ structure. A region of the water-conducting pathway close to the NPA (asparagine-proline-alanine), the AQP signature motif, is shown. The $2F$o-Fc map contoured at 1.5σ is shown as gray mesh, the AQP0 model is shown in yellow with oxygen atoms in red and nitrogen atoms in blue. The red sphere represents a water molecule. (**C**) A diffraction pattern of an untilted AQP0 2D crystal reconstituted at a sphingomyelin:cholesterol ratio of 1:2, showing reflections to better than 1.6-Å resolution. Scale bar indicates $(10 \text{ Å})^{-1}$. (**D**) Density map at 2.5-Å resolution used to build the $AQP0_{1SM:2Chol}$ structure. The same region as in (B) is shown with the same color code. See also Figure 2–figure supplement 1.
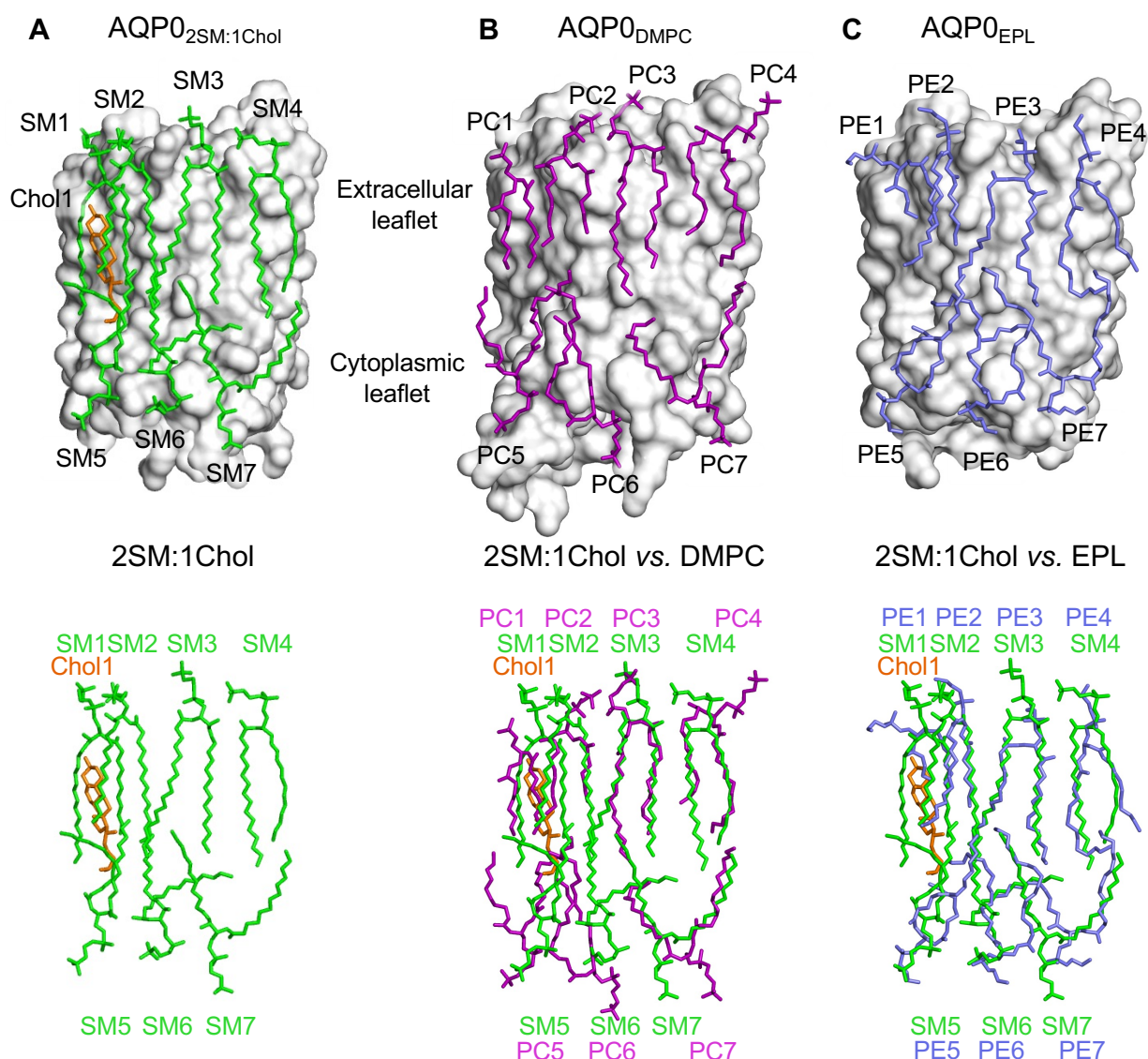
Figure 3. The 2:1 sphingomyelin/cholesterol bilayer surrounding AQP0 is similar to bilayers formed by phosphoglycerolipids. (**A**) The top panel shows the seven sphingomyelins (light green sticks) and one cholesterol (orange sticks) molecules forming the bilayer around an AQP0 subunit (gray surface). The bottom panel shows just the lipid bilayer. (**B**) The top panel shows DMPC lipids (purple sticks) surrounding an AQP0 subunit (Gonen et al., 2005) and the bottom layer shows an overlay of the DMPC bilayer with the 2:1 sphingomyelin/cholesterol bilayer. (**C**) The top panel shows an *E. coli* polar lipids (EPL) bilayer (modeled as PE lipids) (light brown sticks) surrounding an AQP0 subunit (Hite et al., 2010) and the bottom layer shows an overlay of the EPL bilayer with the 2:1 sphingomyelin/cholesterol bilayer. See also Figure 3–figure supplements 1–3 and Table 3.
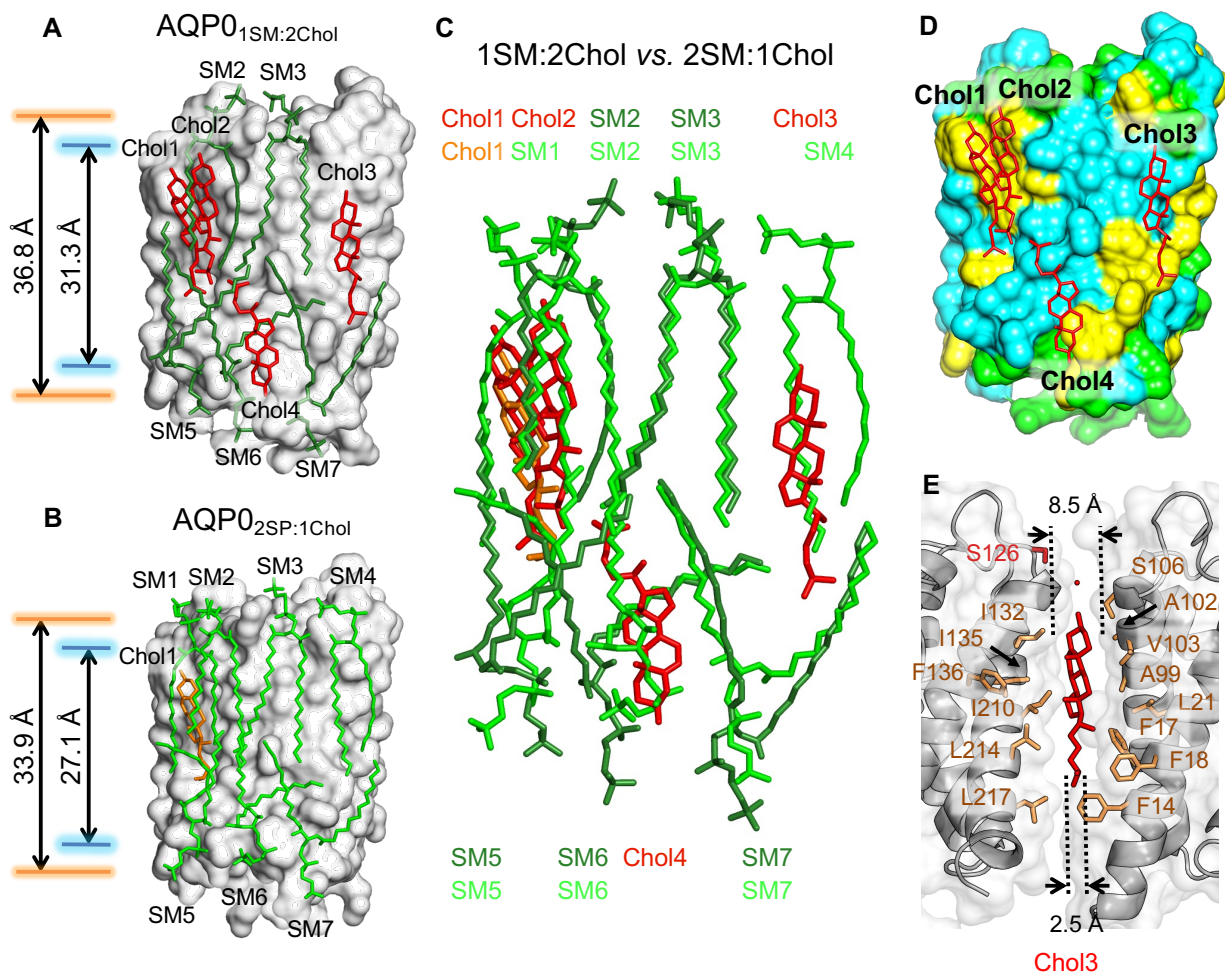
Figure 4. The 1:2 sphingomyelin/cholesterol bilayer surrounding AQP0 and comparison with the 2:1 sphingomyelin/cholesterol bilayer. (**A**) The five sphingomyelins (dark green sticks) and four cholesterol (red sticks) molecules surrounding an AQP0 subunit (gray surface). The arrows between the orange and blue lines indicate the average distances between the phosphorus atoms of the phosphodiester groups and the nitrogen atoms of the amide groups in the two leaflets, respectively. (**B**) The AQP0$_{2SM:1Chol}$ structure shown for comparison with the AQP0$_{1SM:2Chol}$ structure in (A). Arrows as in (A). (**C**) Overlay of the lipid bilayers in the AQP0$_{2SM:1Chol}$ and AQP0$_{1SM:2Chol}$ structures. (**D**) Location of the four cholesterols (red sticks) in the AQP0$_{1SM:2Chol}$ structure with respect to AQP0 surface characteristics. Color coding: yellow, aromatic residues; cyan, hydrophobic residues; and light green, polar and charged residues. (**E**) Position of cholesterol Chol3 (red sticks) in the AQP0$_{1SM:2Chol}$ structure and its interaction with residues of two adjacent AQP0 tetramers (brown sticks). The dotted lines indicate the distance between the two adjacent AQP0 tetramers at the positions of the ring system (~8.5 Å) and the acyl chain (~2.5 Å). See also Figure 4–figure supplements 1–2 and Table 3.
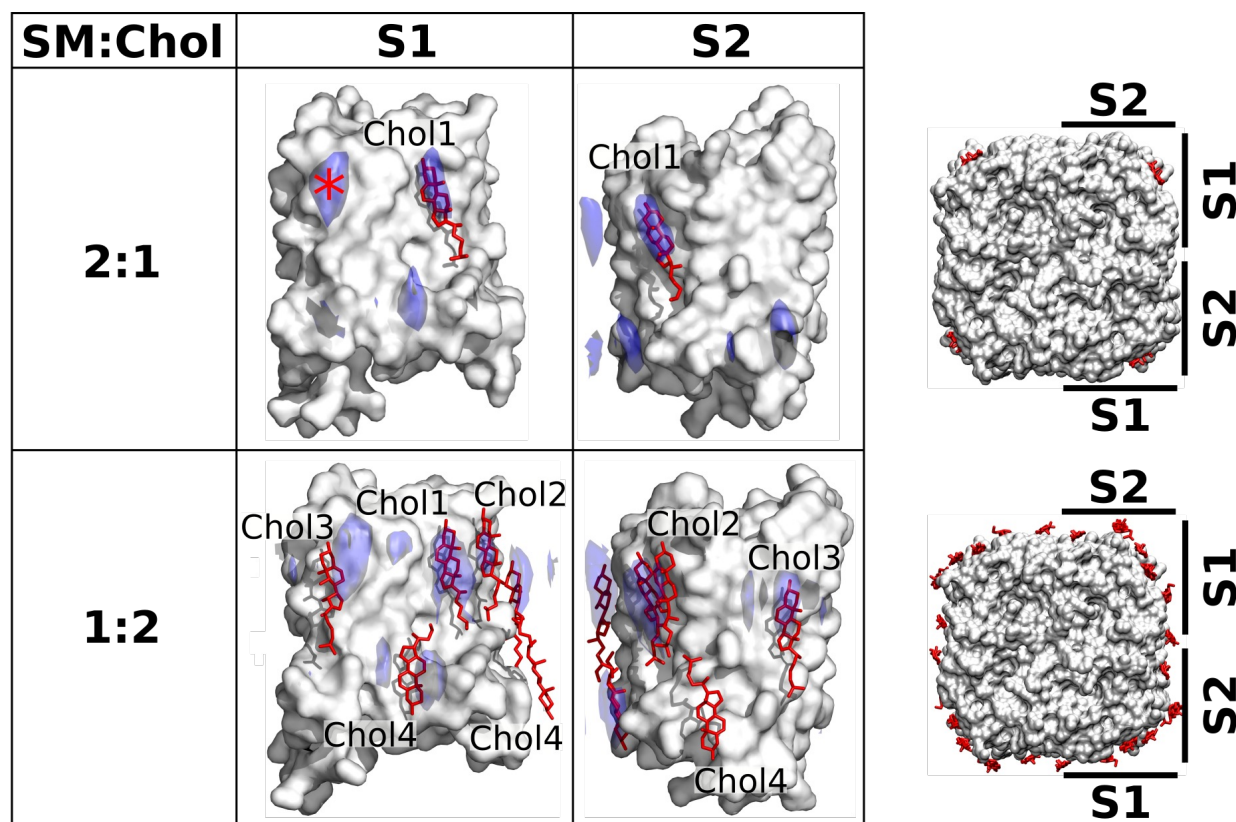
Figure 5. Localization of cholesterol around AQP0 monomers from unbiased MD simulations of individual AQP0 tetramers in SM membranes with low and high cholesterol concentration. Density maps representing the localization of cholesterol around AQP0 over time were computed from simulations starting from unbiased cholesterol positions in membranes at the indicated SM:Chol ratios. After combining the four maps calculated individually for the four subunits of the tetramer, cholesterol densities were projected (blue areas) onto the surface of a single AQP0 monomer (white surface). Projections are shown for the S1 and S2 monomer surfaces, as defined in the representations to the right. Lipids seen in the electron crystallographic structures obtained in membranes at the respective SM:Chol ratios are displayed as sticks and labeled according to the electron crystallographic structures. Densities are contoured at 10σ for the 2:1 SM:Chol membrane and at 9σ for the 1:2 SM:Chol membrane. The density hot spot indicated with an asterisk coincides with the Chol3 position seen at the 1:2 SM:Chol ratio. See also Figure 5– figure supplements 1–3.
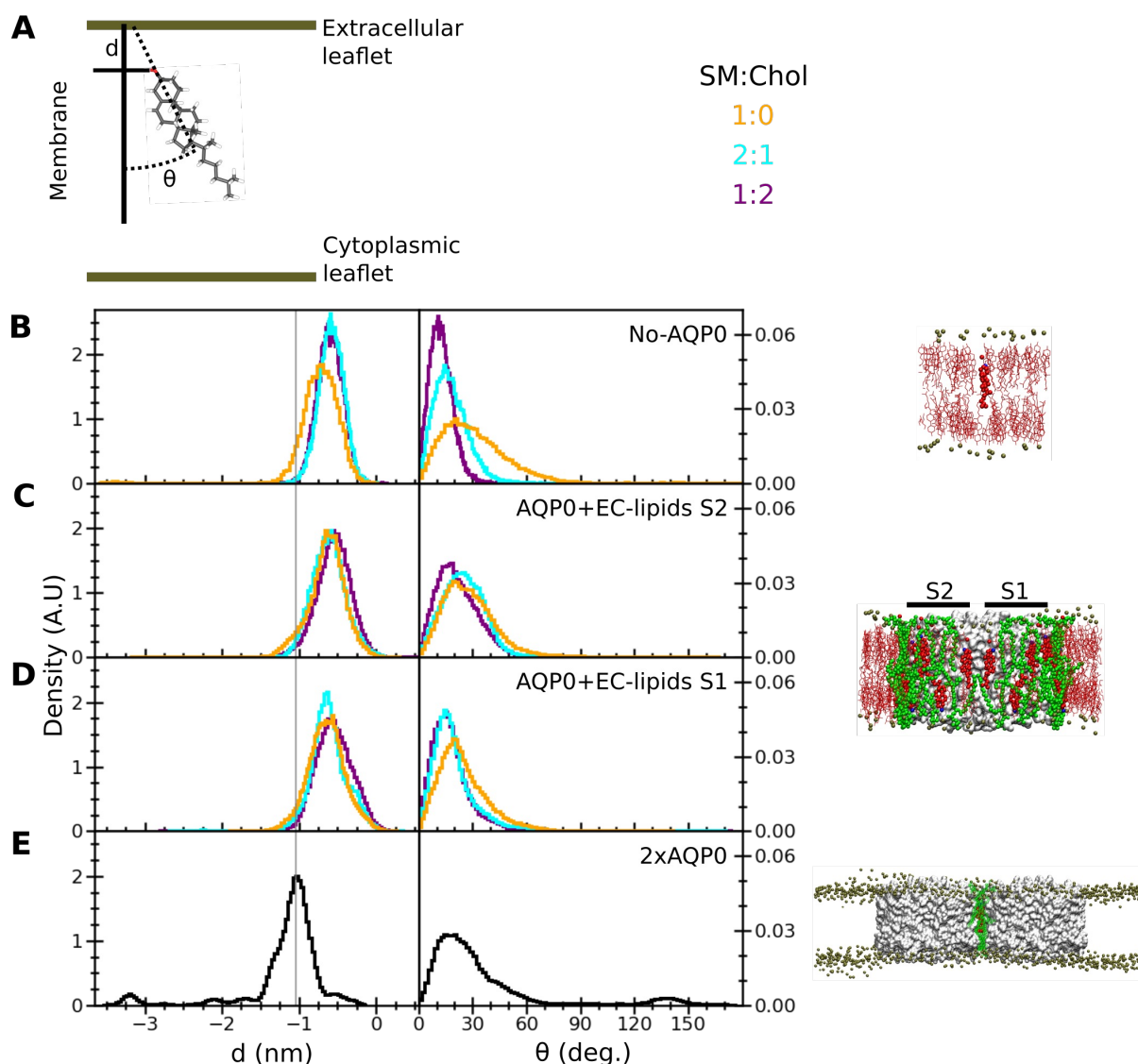
Figure 6. Insertion depth and orientation of a cholesterol at the interface between two AQP0 tetramers. (**A**) Schematic figure illustrating how the insertion depth, d, and orientation angle, θ, of the cholesterol were measured. The cholesterol insertion depth was defined as the distance in z direction of the cholesterol oxygen atom (red stick representation) from the center of mass of the phosphorus atoms of the nearby SM molecules in the extracellular leaflet (top green horizontal line). The cholesterol orientation was defined as the angle between the membrane normal (simulation box z vector) and the vector along the rings of the cholesterol molecule (black dashed line). (**B-E**) Right panels: The three different systems that were simulated, namely (**B**) "No AQP0", a pure lipid membrane without AQP0, (**C, D**) "AQP0 + EC lipids S2/1", a membrane with one AQP0 tetramer surrounded by the annular lipids seen in the AQP0$_{1SM:2Chol}$ structure, and (**E**) "2×AQP0", a membrane containing a pair of AQP0 tetramers together with the lipids in between them from a hybrid AQP0$_{2SM:1Chol}$ structure that replaces the two central SM molecules with the EC deep cholesterol molecules found in the AQP0$_{1SM:2Chol}$ structure. Left panels: Graphs showing normalized histograms for the insertion depth, d, and orientation angle,

70

θ, for the monitored deep cholesterol in membranes with different SM:Chol ratios (see color code in panel **A**), except for the 2×AQP0 system, which was only simulated in a pure SM membrane. For the simulations with one AQP0 tetramer, insertion and orientation were computed separately for the deep cholesterol located at surface S2 (**C**) and S1 (**D**). The vertical line indicates the most probable cholesterol position in the 2×AQP0 system (**E**). See also Figure 6–figure supplement 1.
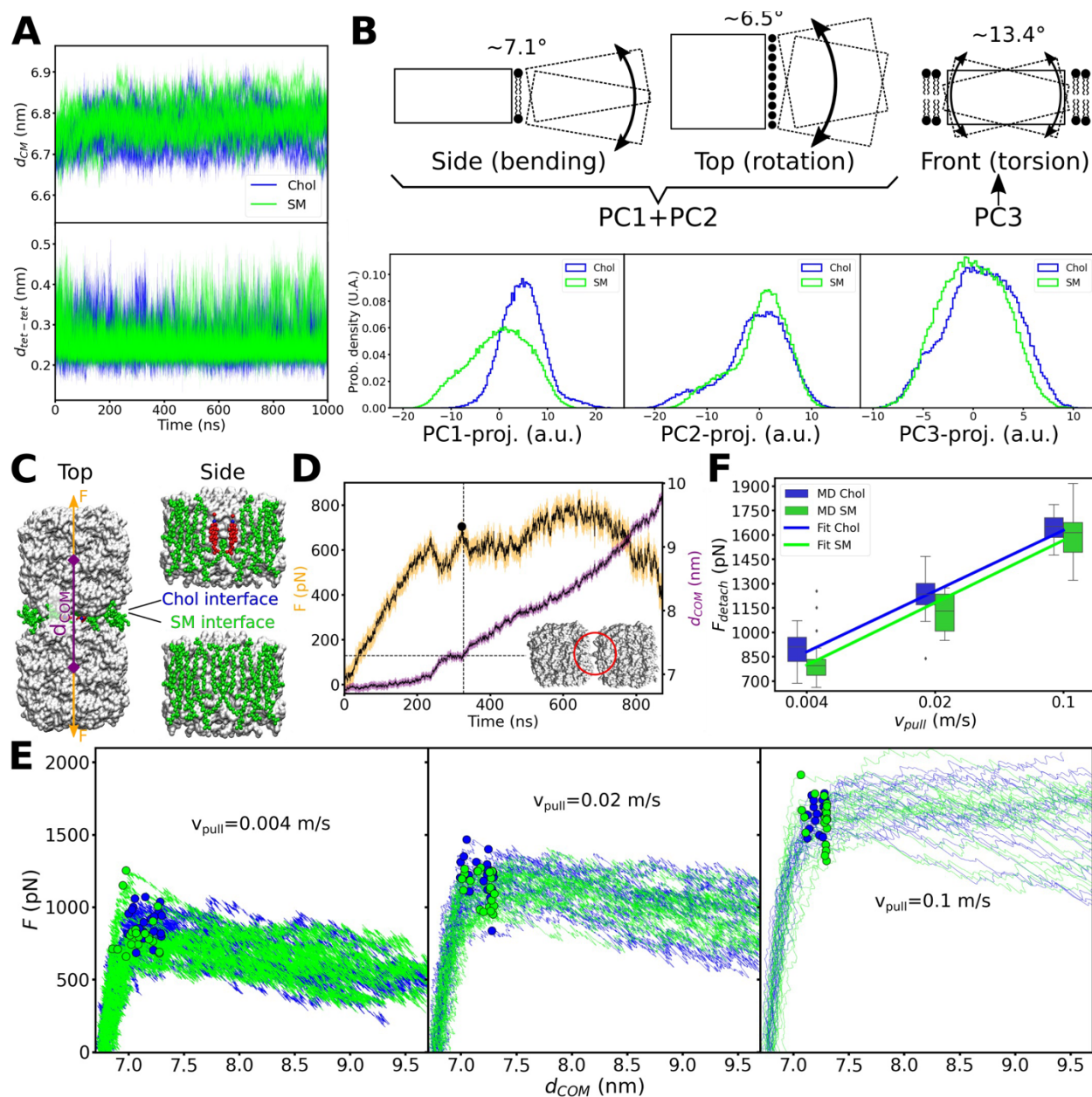
Figure 7. Equilibrium MD simulations of pairs of associated AQP0 tetramers and force-induced separation of two associated AQP0 tetramers. (**A**) Distance between the centers of mass d_{CM} (top) and minimum distance $d_{tet-tet}$ (bottom) between the pair of AQP0 tetramers during the 2×AQP0 simulations in equilibrium for the interface containing only SM molecules (SM, green) and the interface containing the deep cholesterol (Chol, blue) ($n = 10$ simulations for each case). (**B**) Principal component (PC) analysis of the relative movements between the two tetramers. Here, the motion of one of the tetramers (dashed-line rectangle) relative to the other tetramer (solid-line rectangle) was monitored. The three main principal components accounted for 67.9% of the total relative motion between tetramers (PC1: 34.3%, PC2: 24.7%, and PC3: 8.9%). The schematic drawings illustrate the three main modes of motion: bending (depicted in the drawing as viewed from the side of the membrane), lateral rotation (depicted in the drawing as viewed from the top of the membrane), and torsion (depicted in the drawing as viewed from the side of the membrane

with one tetramer in front of the other). Lipids at the interface between the two tetramers (first two panels) and lipids surrounding the two tetramers (last panel) are shown. PC1 plus PC2 capture the bending and rotation while PC3 corresponds to torsion. The histograms in the bottom panels show the projections of the MD trajectories onto the three main PC vectors, for the interfaces containing only sphingomyelin (SM, green) or containing the deep cholesterols (Chol, blue). The approximate angular extent for each of the modes, attributed to these projections, is indicated (in degrees). The distributions with and without cholesterol are very similar, except for PC1. Nevertheless, PC1 relates to a small angular variation (~7.1° bending together with ~6.5° rotation). (**C**) Two AQP0 tetramers (white surface) arranged as in 2D crystals and embedded in a pure SM membrane were pulled apart by exerting a harmonic force F on them in the direction that connects their centers of mass (d_{COM}). Two different interfaces were studied: the "SM interface" consisted solely of SM lipids (green spheres) as seen in the $AQP0_{2SM:1Chol}$ structure, whereas the "Chol interface" contained the deep cholesterols seen in the $AQP0_{1SM:2Chol}$ structure. The reference position of the harmonic springs used to exert the force F was moved at a constant velocity $v_{pull}/2$. (**D**) Force (F) and distance (d_{COM}) time traces are shown for one of the simulations using a v_{pull} of 0.004 m/s. A Gaussian smoothing function (black continuous lines) was applied to the curves (yellow and purple). The detachment force (black circle) was computed as the highest recorded force when d_{COM} started to increase and below a cut-off distance d_{COM} of 7.3 nm (horizontal dashed line indicates the cut-off distance and the vertical dashed line indicated the time when this value was surpassed). Note that using different cut-off distances did not change the overall trend (see Figure 7–figure supplement 1). The inset shows an example of the arrangement of the tetramers at the moment of detachment. The red circle indicates the last contact. (E) Force–distance profiles for the two different interfaces are presented for the three indicated pulling velocities (n = 20 for each case). Dots indicate the point of detachment. (F) Detachment force is presented as a function of the pulling rate for the two interfaces (box plots, n = 20). A fit of the form Fdetach = A + B*log(Vpull) is shown to guide the eye with lines (Fdetach = [2164 + 232*log(Vpull)] for the "Chol" interface and Fdetach = [2116 + 239*log(Vpull)] for the "SM" interface). P-values comparing the two data sets, separately for each pulling velocity, are 0.022 (vpull = 0.004 m/s), 0.015 (vpull = 0.02 m/s), and 0.262 (vpull = 0.1 m/s) (Mann-Whitney U test). Furthermore, a two-way ANOVA test, considering the three pulling velocities at once, retrieved a P-value of 0.003 for the lipid interface change (i.e., Chol vs. SM). See also Figure 7–figure supplement 1.
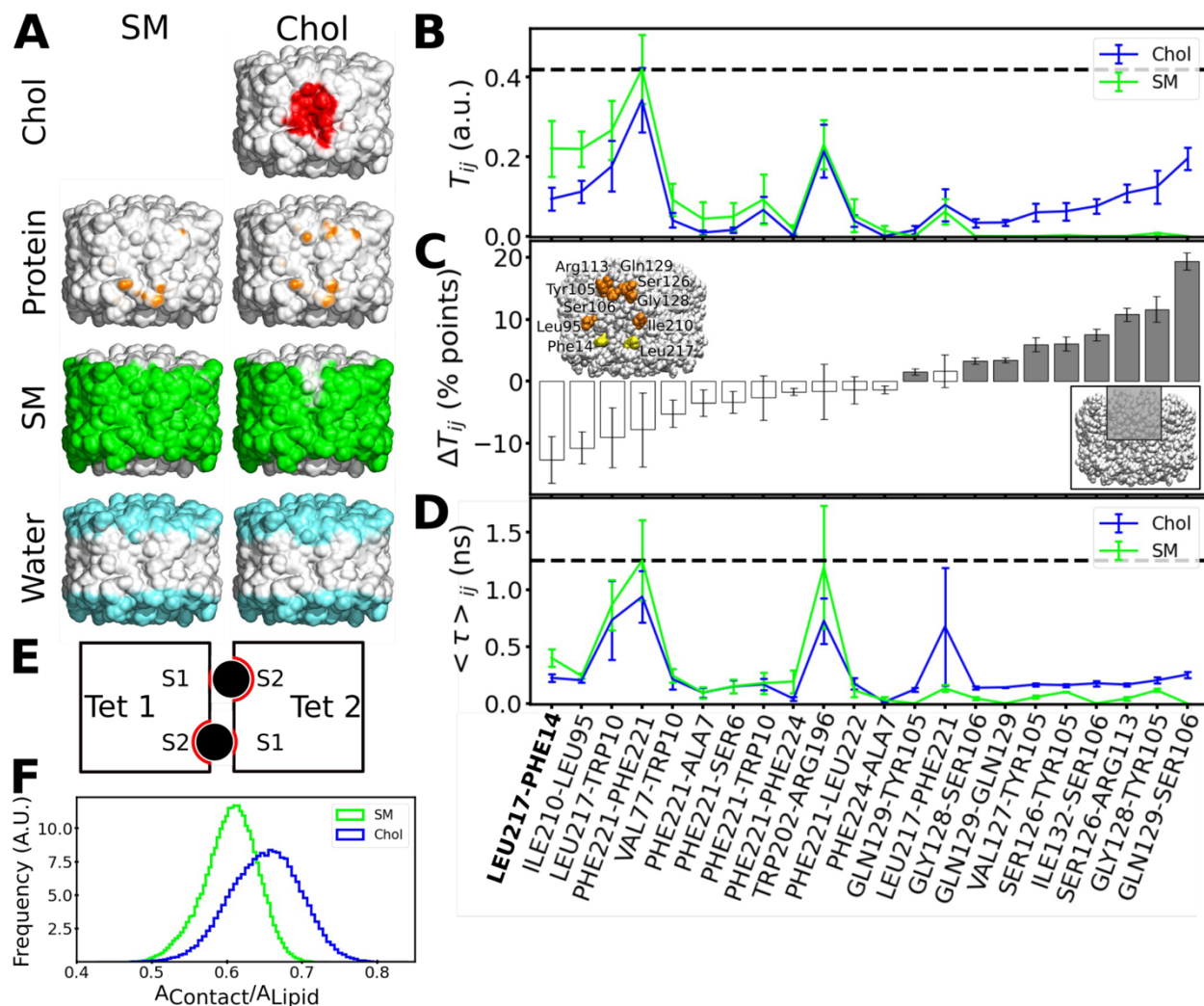
Figure 8. Interactions formed between adjacent AQP0 tetramers and lipid-AQP0 surface complementarity. (**A**) Equilibrium MD simulations were performed with pairs of AQP0 tetramers without cholesterol (left panels) or with cholesterol (right panels) at the interface. Density maps were calculated for different components next to the AQP0 surface over time and these maps were projected onto the surface of one of the AQP0 tetramers to represent their localization. For clarity, the second tetramer, which would be in front of the shown tetramer, is not shown. The density displayed at arbitrary density units is color-coded and shows the position of cholesterol (red), protein, i.e., the neighboring AQP0 tetramer (brown), sphingomyelin (green) and water (blue). (**B**) T_{ij} is defined as the fraction of time during which residues (i, j) from opposite tetramers are in contact. This quantity was extracted from the equilibrium simulations for the pure sphingomyelin interface $T_{ij}(SM)$ and for the interface containing cholesterol $T_{ij}(Chol)$. $T_{ij} = 0$ means that i and j were never in contact and $T_{ij} = 1$ means that they were always in contact. (**C**) The pairwise difference $\Delta T_{ij} = T_{ij}(Chol) - T_{ij}(SM)$ is shown, discarding insignificant changes ($\Delta T_{ij} < 1$ percentage, %, points). Accordingly, a value of $\Delta T_{ij} > 0$ ($\Delta T_{ij} < 0$) corresponds to protein–protein contacts that were more often observed in the simulations with cholesterol (sphingomyelin). For instance, the residue pair Gln129–Ser106 was observed almost 20 percentage points more time in the simulations with cholesterol. The color of the bars

indicates the location of the residues (grey: inner part of the extracellular leaflet, i.e., where deep cholesterol resides; white: the rest of the interfacial protein surface, see inset at lower right). Residues involved in a high $\Delta T_{ij} > 10$ percentage points are highlighted in orange in the inset (yellow for the contact Leu217–Phe214 observed in the electron crystallographic structure). (**D**) The average duration for every established protein–protein contact, $\langle\tau\rangle_{ij}$, is also displayed for the two different lipid interfaces. In (**B**) and (**D**), the horizontal dashed lines indicate the highest value observed for all possible residue pairs. Contacts observed in the electron crystallographic structures are highlighted in bold letters. In B–D, the avg±s.e.m. is presented ($n = 20$, i.e., 10 independent simulation times with 2 symmetric monomeric interfaces). (**E**) The schematic drawing depicts a top view of the two associated AQP0 tetramers (squares, "Tet 1" and "Tet 2") with the two central lipids sandwiched between them (black circles). The other lipids at the interface are not shown for clarity. The respective monomer surfaces S1 and S2 are indicated. The region of the surface of the two tetramers that is in total covered by a lipid, $A_{Contact}$ (red line) was normalized by the surface area of the lipid, A_{Lipid} (here corresponding to the perimeter of the circles). This ratio gives a measure of the surface complementarity between the tetramers and the sandwiched lipids, i.e., the higher the value of $A_{Contact}/A_{Lipid}$ the more the two surfaces complement each other. (**F**) Normalized histograms of $A_{Contact}/A_{Lipid}$ obtained from the equilibrium MD simulations are shown for the central sphingomyelin (SM) and cholesterol (Chol). See also Figure 8–figure supplements 1–3.
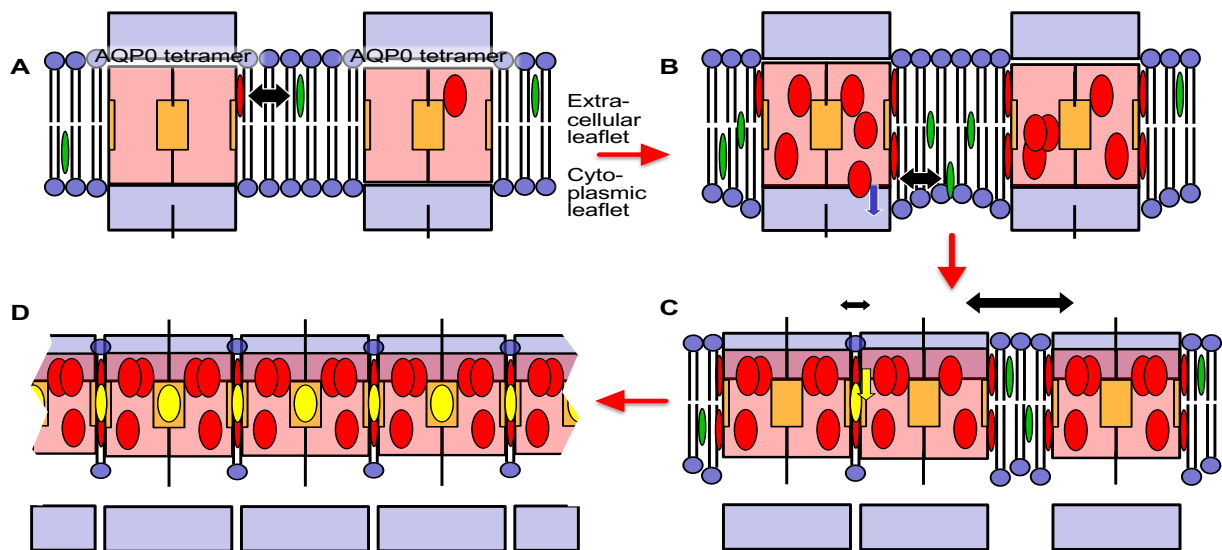
Figure 9. Proposed model for how an increasing cholesterol concentration drives AQP0 2D array formation in the native lens membrane. (**A**) At a low cholesterol concentration, AQP0 tetramers are mostly surrounded by phospholipids and sphingomyelin. Free cholesterol in the membrane (green ovals) only associates with the highest affinity cholesterol-binding sites. Cholesterols occupying these peripheral binding sites are shown as red ovals and the black double-headed arrow indicates the transient nature of this interaction. The deep cholesterol-binding sites (orange squares) are not occupied. (**B**) With increasing cholesterol concentration, more cholesterols associate with the AQP0 surface. These cholesterols cause the interacting lipids in the cytoplasmic leaflet to move out from the bilayer center (blue arrow), resulting in the annular lipid shell that has a bigger hydrophobic thickness than the surrounding membrane, creating a hydrophobic mismatch that results in membrane deformation. (**C**) To minimize hydrophobic mismatch, AQP0 tetramers cluster. Cholesterol in between adjacent tetramers can move into the deep binding sites (yellow arrow) and cholesterol occupying deep binding sites (yellow ovals) act as glue that increases that association of the adjacent tetramers (indicated by the small double-headed black arrow) as compared to adjacent tetramers that do not sandwich a deep-binding cholesterol (indicated by the large double-headed black arrow). Clustering of proteins to minimize hydrophobic mismatch and stabilization by deep cholesterol-mediated protein–protein interactions may be the basis for the formation of transient lipid rafts. (**D**) Each AQP0 tetramer has four deep cholesterol-binding sites. As a result of the avidity effect, AQP0 can form large and stable 2D arrays.